




## Subcritical axisymmetric solutions in rotor-stator flow

Artur Gesla <sup>\*</sup>*Sorbonne Université, F-75005 Paris, France*Yohann Duguet  and Patrick Le Quéré *LISN-CNRS, Université Paris-Saclay, F-91400 Orsay, France*Laurent Martin Witkowski *Université Claude Bernard Lyon 1, CNRS, Ecole Centrale de Lyon, INSA Lyon, LMFA, UMR5509, 69622 Villeurbanne, France*

(Received 18 December 2023; accepted 3 July 2024; published 13 August 2024)

Rotor-stator cavity flows are known to exhibit unsteady flow structures in the form of circular and spiral rolls. While the origin of the spirals is well understood, that of the circular rolls is not. In the present study the axisymmetric flow in an aspect ratio  $R/H = 10$  cavity is revisited numerically using recent concepts and tools from bifurcation theory. It is confirmed that a linear instability takes place at a finite critical Reynolds number  $Re = Re_c$  and that there exists a subcritical branch of large amplitude chaotic solutions. This motivates the search for subcritical finite-amplitude solutions. The branch of periodic states born in a Hopf bifurcation at  $Re = Re_c$ , identified using a self-consistent method (SCM) and arclength continuation, is found to be supercritical. The associated solutions only exist, however, in a very narrow range of  $Re$  and do not explain the subcritical chaotic rolls. Another subcritical branch of periodic solutions is found using the harmonic balance method with an initial guess obtained by SCM. In addition, edge states separating the steady laminar and chaotic regimes are identified using a bisection algorithm. These edge states are biperiodic in time for most values of  $Re$ , where their dynamics is analyzed in detail. Both solution branches fold around at approximately the same value of  $Re$ , which is lower than  $Re_c$  yet still larger than the values reported in experiments. This suggests that, at least in the absence of external forcing, sustained chaotic rolls have their origin in the bifurcations from these unstable solutions.

DOI: [10.1103/PhysRevFluids.9.083903](https://doi.org/10.1103/PhysRevFluids.9.083903)

### I. INTRODUCTION

Rotating flows in closed containers have motivated many hydrodynamic stability studies due their simplicity, their relevance to various industrial configurations and the dramatic patterns observed [1,2]. Hydrodynamic stability theory itself has long rested on the difference between open and closed flow geometries, which leads respectively to the opposition between local and global methods of analysis [3]. The case of cylindrical containers, with a finite radius much larger than their height, falls somewhat in between, and it is not always clear which kind of analysis is most relevant: global mode analysis, where all modes are consistent with the boundary conditions, or the (often simpler) local analysis of perturbations as in infinitely extended systems. We consider in this study the incompressible flow between a rotor and a stator, in the case where the lateral

---

<sup>\*</sup> Also at LISN-CNRS, Université Paris-Saclay, F-91400 Orsay, France.

circular wall rotates together with the rotor. This flow was investigated in the late 1990s in detail, mainly using experimental facilities [4–7] but also later two-dimensional and three-dimensional numerical computations [4,7–11]. The flow is characterized by two independent parameters: a Reynolds number  $Re$  proportional to the rotor’s angular velocity  $\Omega$ , and a geometrical aspect ratio  $\Gamma = R/H$  where  $H$  and  $R$  are the respective height and radius of the cylinder. The base flow for the configuration of interest here, where  $\Gamma \geq 5$ , is axisymmetric. It has a dominantly azimuthal flow with strong shear at the walls, as well as a meridional recirculation, associated, for high enough  $Re$ , with two separated boundary layers, one along the stator (labeled as the Bödewadt boundary layer) and the other along the rotor (labeled as the Ekman boundary layer).

The linear stability of this axisymmetric flow with respect to three-dimensional perturbations was carried out by Gelfgat [11]. The predictions are in very good agreement with experiments [6,12] as well as with direct numerical simulations [13]. The linear instability from which spiral patterns originate [11] is a supercritical Hopf bifurcation. The resulting patterns saturate in amplitude and rotate around the cavity at an angular velocity smaller than that of the rotor. Yet, although well understood these beautiful spiral patterns are not the earliest manifestation of unsteadiness encountered as  $Re$  is increased from zero. As reported in most experimental studies so far, *axisymmetric ringlike perturbations* are also observed. Viewed in a meridional plane they correspond to wave packets of vortices located near the stator. At low enough  $Re$  close to their experimental onset they are simply convected inwards and disappear as they pass near the axis before they reach the rotor [6]. At higher  $Re$  the rolls described in [5] form a steady front with complex internal dynamics. Adopting a locallike description, these rings are usually described as emerging from a convective instability of the Bödewadt layer, developing from the corner, and propagating inwards along the stator until the axis region where they are damped [7]. Note that for larger  $Re$ , there is a mix of spiral and circular rolls. As far as experiments and numerics can be quantitatively compared, an axisymmetric instability was reported in Ref. [8] at  $Re \approx 2950$ . This has to be contrasted with the experimental values: rings are reported for  $Re$  as low as 180 [6] and 160 [5] for a similar aspect ratio (using the same definition of  $Re$ ). The configuration with  $\Gamma = 5$  has been also simulated using accurate spectral codes [9,14], although the circular patterns reported in these studies are transients. The simulated ring patterns are more clearly sustained in case the rotation of the disk is temporally modulated [15]. It is hence tempting to interpret them as a (linear) response to external forcing, in other words *not* as a genuine nonlinear state of the system. References [9,15] as well as [7] support the view that these vortical structures are only transient responses to external effects. The overlooked investigation by Daube and Le Quéré [8] goes beyond by identifying, now for  $\Gamma = 10$ , three new properties: (i) a linear instability respecting the axisymmetry of the flow was identified using eigenvalue, at a value of  $Re$  above that where rings can be observed, (ii) quantitatively huge levels of transient growth before (iii) the ring patterns saturate in amplitude, and (iv) the existence of a subcritical large amplitude chaotic solution branch. These new features, especially (i) and (ii) are familiar to the subcritical shear flow community working on plane Poiseuille and boundary layer flows [16,17].

Several questions can be asked at this point: is the critical point of Daube and Le Quéré confirmed and how robust is it? Does a branch of axisymmetric nonlinear states bifurcate subcritically from this point? Is it physically consistent with the convective instability put forward by experimentalists? The lack of radial propagation of the associated envelope, attested from experimental space-time diagram, suggests that nonlinearity can enter the picture. Adopting such a point of view, the quasisteady envelopes of rings could be interpreted as genuinely nonlinear states, with a complex time dependency but a coherent spatial structure. This should be contrasted with the concept of noise-sustained coherent structure [7,18]. The subcriticality of the ring regime and the presence of an axisymmetric instability threshold, both reported in Ref. [8], would make the nonlinear branch emerging from the critical point, if it is confirmed to also bifurcate subcritically, the ideal candidate to explain experimental observations. Subcriticality would also imply that, for  $Re < Re_c$ , only finite-amplitude perturbations above a certain threshold can excite this nontrivial regime.

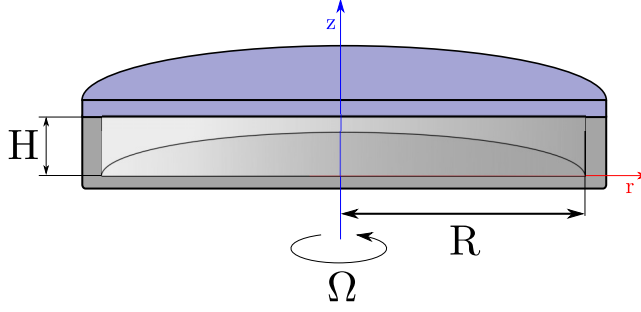


FIG. 1. Rotor-stator geometry with rotating shroud. The setup is characterized by the Reynolds number  $Re = \Omega H^2 / \nu$  and an aspect ratio  $\Gamma = R/H$  fixed here to 10.

In order to shed a light on the interrogations above, the present numerical work aims at better characterizing the stability threshold and its numerical robustness, at identifying for the first time nonlinear branches of solutions possibly connected to the critical point, and at debating whether the corresponding nonlinear states bear any relation with the patterns observed experimentally and numerically. Among all possible nonlinear states that can exist beyond the laminar base flow, many nonlinear solutions of the subcritical regime are unstable. Some of them possess the property of lying on the laminar-turbulent boundary, the so-called *edge* manifold in the associated state space. Numerical simulations constrained to lie in that manifold converge asymptotically to specific equilibrium regimes called *edge states*. Their determination is specifically interesting for subcritical transition since their instability captures the mechanisms leading from finite-amplitude initial perturbations of the base flow towards the turbulent state. We focus here on the same flow, restricted to the axisymmetric subspace, in a cavity of aspect ratio  $\Gamma = 10$  as in Ref. [8]. As will become clear throughout the paper, many traditional numerical algorithms turn out to be technically too limited for the search of nonlinear states. This represents an opportunity to improve them or to use recent methods whose relevance will be also discussed.

The paper is structured according to the following plan: Sec. II describes briefly the numerical methods used, Sec. III describes the laminar base flow and its stability, Sec. IV describes the nonlinear periodic states found in the flow, Sec. V describes the edge tracking and the edge state dynamics, and finally Sec. VI summarizes the results and gives outlooks for future work.

## II. NUMERICAL METHODS

### A. Flow configuration

The system under consideration is an axisymmetric rotor-stator flow. The two-dimensional meridional geometry is depicted in Fig. 1. The flow is governed by the incompressible Navier-Stokes equations (1a) and (1b) written in polar coordinates  $(r, z)$ , with the velocity  $\mathbf{u}$  characterized by its three components  $(u_r, u_\theta, u_z)$ :

$$\frac{\partial \mathbf{u}}{\partial t} + (\mathbf{u} \cdot \nabla) \mathbf{u} = -\frac{1}{\rho} \nabla p + \nu \nabla^2 \mathbf{u}, \quad (1a)$$

$$\nabla \cdot \mathbf{u} = 0 \quad (1b)$$

together with the boundary conditions (2)

$$\begin{aligned} \mathbf{u} &= r\Omega \mathbf{e}_\theta, & \text{at the rotor } (z = 0) \\ \mathbf{u} &= R\Omega \mathbf{e}_\theta, & \text{at the shroud } (r = R) \\ \mathbf{u} &= \mathbf{0}, & \text{on the stator } (z = H), \end{aligned} \quad (2)$$

TABLE I. Uniform ( $600 \times 160$  cells in  $r$ - $z$ ) and nonuniform ( $1024 \times 192$  cells in  $r$ - $z$ ) mesh used in the study.  $dr$  and  $dz$  correspond to the horizontal and vertical dimension of the pressure cell in the finite volume discretization.

$N_r \times N_z$	Type	max $dr$	min $dr$	max $dz$	min $dz$
$600 \times 160$	Uniform	0.0167	–	0.0062	–
$1024 \times 192$	Nonuniform	0.0114	0.0028	0.0083	0.0017

where  $\Omega$  is the angular frequency of the disk rotation,  $\nu$  is the kinematic viscosity of the fluid and  $\rho$  its density. As in [8], the geometry is characterized by a radius-to-gap ratio  $\Gamma = R/H$  equal to 10. Nondimensionalization of all lengths, and of the velocity field  $\mathbf{u}$  is achieved respectively using the lengthscale  $H$  and velocity scale  $\Omega H$ , without change of notation. Different possible definitions for the Reynolds number  $Re$  include  $Re_R = \Omega R^2/\nu$ , built on the length scale  $R$ ,  $\Omega H^{3/2} R^{1/2}/\nu$  when the centrifugal force is the key destabilizing mechanism as is the case in exactly counter-rotating disks [19], or  $Re_{RH} = \Omega RH/\nu$ . In this study  $Re_H = \Omega H^2/\nu$ , related to the length scale  $H$ , is chosen.

### B. Spatial discretization

The continuous problem is discretized using a second order finite volume method on a staggered grid. The details of the discretization as well as the staggered arrangement can be found, for instance, in Appendix of Ref. [20]. Two types of meshes, uniform and nonuniform, are used in the present study. The uniform mesh on one hand allows for direct, reproducible and easy comparison with the existing literature. The nonuniform mesh, on the other hand, allows for greater accuracy at the price of only a moderate increase in computational cost. The nonuniform mesh is refined in the regions near the rotor, the stator, and the rotating shroud. In the radial direction it is uniform from  $r = 0$  to  $r = 8$  and then refined on the remaining  $r \in (8, 10)$  according to the formula

$$b_i = \frac{1}{2} \left( 1 + \frac{\tanh[\delta(x_i - \frac{1}{2})]}{\tanh(\delta/2)} \right), \quad (3a)$$

$$r_i = 8 + 2 \frac{b_i}{[a + (1-a)b_i]} \quad (3b)$$

with  $\delta = 0.7258$  and  $a = 0.4989$ , where  $x_i \in (0, 1)$  is the uniform mesh. Here 70% of total number of  $N_r$  grid points are used in the uniform region  $r \in (0, 8)$ , and the remaining 30% are used in the nonuniform region  $r \in (8, 10)$ . The nonuniform mesh in the axial direction follows the formula

$$z_i = \frac{1}{2} \left( 1 + \frac{\tanh[\delta(\frac{i}{N_z} - \frac{1}{2})]}{\tanh(\delta/2)} \right) \quad (4a)$$

with  $\delta = 2.8587$ . Details on the resulting cell size for the pressure are given for two mesh types in Table I. In both the uniform and nonuniform case, the number of points in the radial direction  $r$  (resp. the axial direction  $z$ ) is noted  $N_r$  (resp.  $N_z$ ).

### C. Numerical simulation

Time integration is carried out using a Backwards Differentiation Formula 2 scheme (BDF2). It uses a prediction-projection algorithm in the rotational pressure correction formulation, as described in [21]. The diffusion term treated implicitly gives rise to a Helmholtz problem for each velocity component increment. These Helmholtz problems are solved using an alternating-direction implicit (ADI) method in incremental form which preserves the second-order accuracy in time. In the projection step the velocity field is projected onto the space of divergence-free fields by solving a Poisson equation for pressure. This Poisson equation is solved using a direct sparse solver. Time

integration is performed with a time step  $dt$  corresponding to a Courant-Friedrichs-Lewy (CFL) number of 0.3.

The nonlinear system of Eqs. (1) and (2) admits for all  $Re$  a steady solution also called  $(U_b, P_b)$ . Once the system is discretized, the solution of the large algebraic nonlinear system of equations is determined numerically using a Newton-Raphson algorithm. The  $O(4N_r N_z)$  unknowns are the velocity and pressure values at each discretization point. The linear stability of the base flow is evaluated using the Arnoldi method based on a well-validated ARPACK package [22]. The shift-and-invert mode is used to find the interesting subset of the eigenvalues. For a generalized eigenvalue problem

$$A\mathbf{w} = \lambda B\mathbf{w}, \quad (5)$$

the shift-and-invert method finds a subset of eigenvalues closest to a complex shift  $s$  by repeated Arnoldi iteration:

$$\nu \mathbf{w} = (A - sB)^{-1} B\mathbf{w} \quad (6)$$

where the original eigenvalues  $\lambda$  can be retrieved with

$$\nu = \frac{1}{\lambda - s}. \quad (7)$$

We take advantage of the finite volume discretization which leads to sparse matrices. Building and storing explicitly the matrix associated with the Jacobian matrix is not a problem since the number of nonzero elements scales with the number of grid points. Most techniques used to compute the base flow and the associated eigenmodes are similar to those presented in Appendix B of [20]. The main change is the use of MUMPS [23] as the direct solver for the linear system at each iteration step of Newton-Raphson algorithm. Due to the presence of the thin boundary layers close to each disk, the set of equations resulting from the discretization of the continuous system is in general poorly conditioned. Sparse direct solvers will be therefore preferred over iterative solvers. Once  $(U_b, P_b)$  is found, the time-stepping code can be adapted to evolve the perturbation to the base flow rather than the full velocity field itself, at the expense of a triple evaluation of the convective terms.

Two recently developed methods are additionally used in this study: the self-consistent method (SCM) introduced in [24] and the Newton method for converging periodic orbits, similar to the algorithm described in [25,26]. Those will be briefly explained in Sec. IV.

### III. STABILITY OF THE BASE FLOW

#### A. Base flow and critical Reynolds number

The first step in the analysis of the present flow case is to identify numerically the steady base flow and to study its stability as a function of the Reynolds number  $Re$ . The base flow  $(U_b, P_b)$  is shown for  $Re = 3000$  in Fig. 2. The base flow features, as expected, shear due to axial gradients of azimuthal velocity, and a meridional recirculation. The structure of the base flow has been investigated in detail in Ref. [27]. For high enough  $Re$ , the base flow is formally self-similar in an  $O(1)$  region around the axis, with the bulk in solid body rotation, with a rotation velocity 0.313. A snapshot of the azimuthal velocity is shown (in perturbation mode) for the chaotic rolls at the same value of  $Re$  in Fig. 2(c). The vortical structures are mainly located between  $r = 1$  and 6. Occasional ejections of fluid from the Bödewadt layer can be seen, for instance, in Fig. 2(c) for  $4 < r < 6$ .

The stability of the base flow is studied by introducing infinitesimal perturbation to the velocity and pressure fields in the following form:

$$\mathbf{u} = \mathbf{U}_b + \mathbf{u}' e^{\lambda t} + \mathbf{u}'' e^{\lambda^* t}, \quad p = P_b + p' e^{\lambda t} + p'' e^{\lambda^* t}. \quad (8)$$

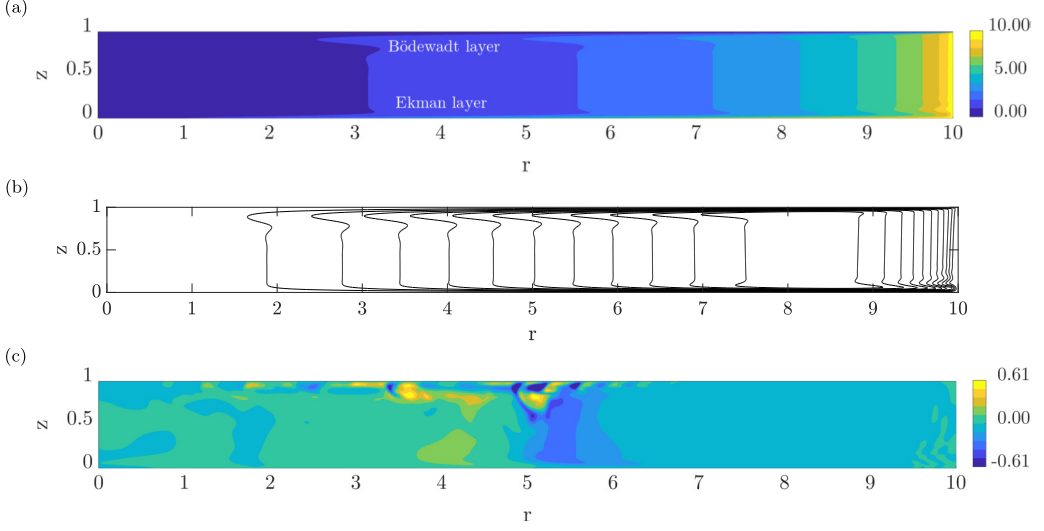


FIG. 2. (a) Azimuthal velocity for the base flow, (b) streamfunction associated with the meridional base flow for  $\psi = 0$  at the wall to 0.6 with increments for isovalues of 0.05, and (c) instantaneous azimuthal velocity perturbation for chaotic rolls.  $\text{Re} = 3000$ . The rotating walls are on the right and at the bottom, the stationary wall at the top, and the left boundary corresponds to the symmetry axis. The streamfunction  $\psi(r, z)$  is defined implicitly by  $u_r = \frac{1}{r} \frac{\partial \psi}{\partial z}$  and  $u_z = -\frac{1}{r} \frac{\partial \psi}{\partial r}$ .

The asterisk denotes complex conjugate. Plugging this *ansatz* into the Navier-Stokes equations and linearizing around  $(\mathbf{U}_b, P_b)$  yields the new system

$$\lambda \mathbf{u}' + (\mathbf{u}' \cdot \nabla) \mathbf{U}_b + (\mathbf{U}_b \cdot \nabla) \mathbf{u}' = -\nabla p' + \frac{1}{\text{Re}} \nabla^2 \mathbf{u}', \quad (9a)$$

$$\nabla \cdot \mathbf{u}' = 0. \quad (9b)$$

After spatial discretization the above system can be recast into the generic form

$$\mathbf{J} \mathbf{q}' = \lambda \mathbf{B} \mathbf{q}', \quad (10)$$

where  $\mathbf{q}' = (u'_r, u'_\theta, u'_z, p')$ ,  $\mathbf{J}$  is the Jacobian evaluated on the base flow  $(\mathbf{U}_b, P_b)$  and  $\mathbf{B}$  is the identity matrix except for the rows corresponding to the continuity equation. The eigenvalues  $\lambda$  ( $=\lambda_r + i\lambda_i$ ) of the generalized eigenproblem (10) are found numerically using the ARPACK library in the shift-invert mode. For each shift  $\sigma = 0.1i, 0.5i, 1.0i, 2.0i$ , a fixed number of 200 of eigenvalues is found. The mesh used in the above example was chosen uniform with  $N_r \times N_z = 600 \times 160$  as in [8]. Part of the resulting spectrum is shown in Fig. 3 for two values of  $\text{Re} = 2900$  and  $3000$ , respectively, below and above the instability threshold. The base flow and the associated least stable eigenvector for  $\text{Re} = 3000$  are visualized in Figs. 2(a) and 4(a)–4(b), respectively. This eigenvector consists mainly of a steady wave packet of counter-rotating rolls localized inside the Bödewadt layer. The largest amplitude of these rolls corresponds to  $1 \leq r \leq 2$ . Weaker yet larger-scale wavelike structures can also be observed outside the Bödewadt layer, displaying various inclinations depending on the radial position. They are interpreted as eigen-oscillations due to the rotation of the core, like inertial waves (whose wavevector's orientation is directly dependent on the ratio between angular frequency and rotation rate) except that the rotation rate varies spatially, like in other nonconfined vortical flows [28]. Both the rolls and the wavelike structure make up the oscillatory eigenmode. For clearer evidence about the relevance of inertial oscillations to the eigenmodes, we illustrate in Fig. 4(c) another eigenmode from the spectrum at  $\text{Re} = 3000$ , with angular frequency  $\lambda_i \approx 0.5$  smaller than for the leading eigenmode. This eigenmode does not feature

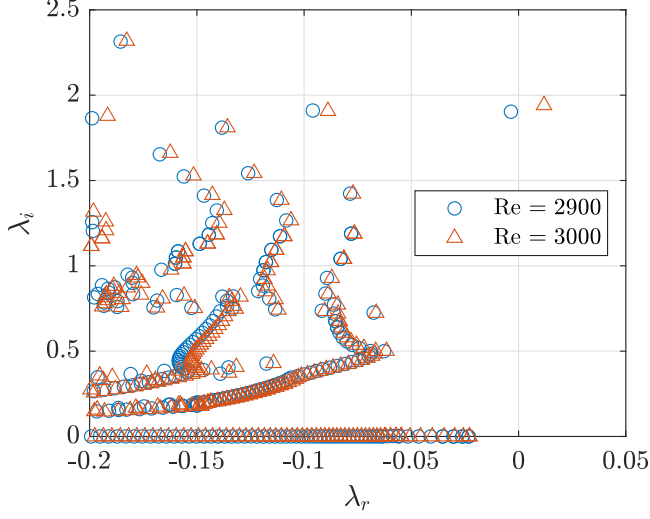


FIG. 3. Spectrum of the linearized Navier-Stokes operator in the generalized eigenvalue problem (10) for two values of  $Re = 2900$  and  $Re = 3000$  straddling  $Re_c$ . The eigenvalue crossing the imaginary axis defines the unstable eigenmode of the flow. Spatial resolution  $R0$  (see Table V).

any roll structure inside the Bödewadt layer but features energetic oblique structures with a tighter angle consistently with the expected behavior for inertial waves. A more detailed investigation of inertial wave contributions to enclosed rotating flows is left for a specific study.

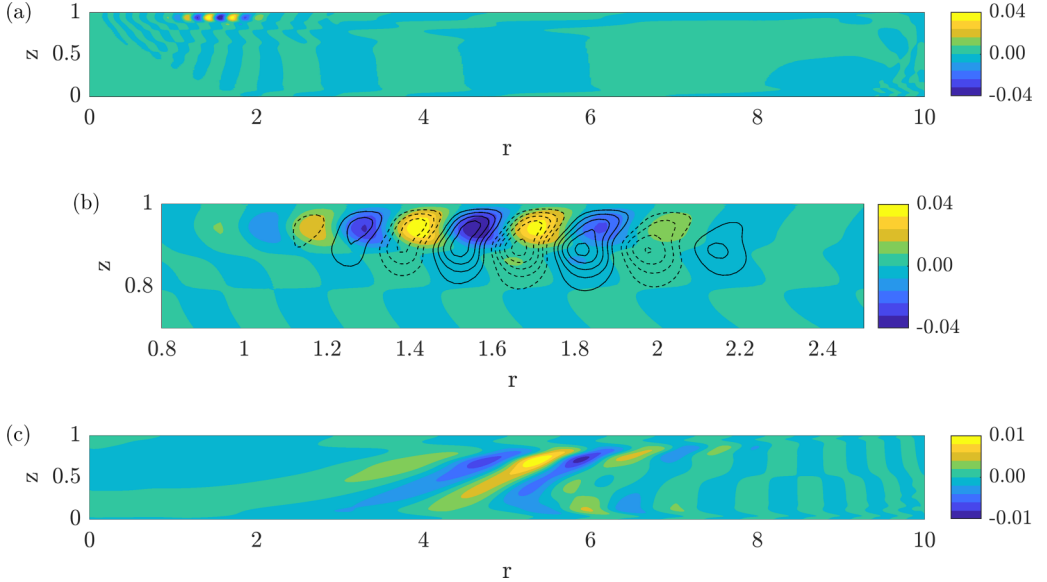


FIG. 4. (a) Azimuthal velocity component of the unstable eigenvector at  $Re = 3000$ , (b) zoom of (a) with streamfunction isocontours superimposed for  $\psi' = -2.5 \times 10^{-4}$  to  $2.5 \times 10^{-4}$  with increments for isocontours of  $5 \times 10^{-5}$  (negative values are dashed lines), and (c) same as (a) for another eigenmode for  $Re = 3000$  with  $\lambda = -0.062 + 0.49i$ . Resolution  $R0$  (see Table V).



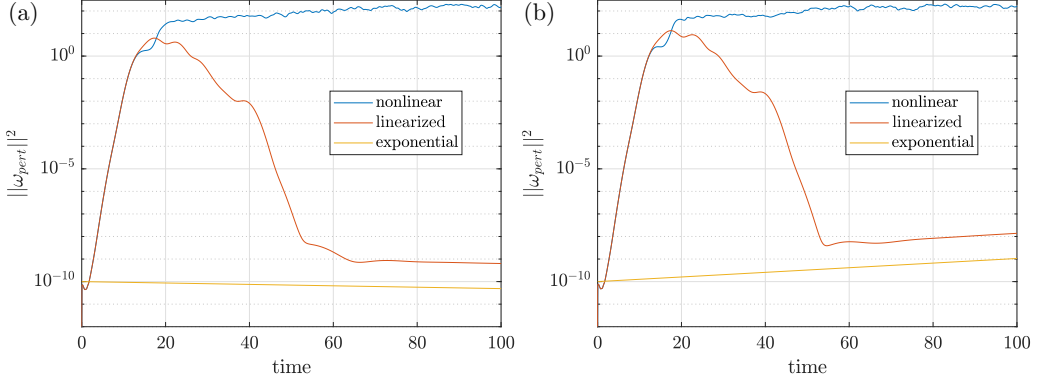


FIG. 5. Time evolution of the observable  $a^2 (= \|\omega_{\text{pert}}\|^2)$  in linear and nonlinear time integration at  $\text{Re} = 2900 < \text{Re}_c$  (a) and  $\text{Re} = 3000 > \text{Re}_c$  (b). The slope of the late time evolution of the observable in the linear code is compared with the exponential growth  $\propto \exp(2\lambda_r t)$  associated with the least stable eigenmode. Spatial resolution R0.

### B. Non-normality of the linearized dynamics

As noted in [8] the dynamics linearized around the base flow in the rotor-stator cavity is strongly non-normal. To assess the strength of the non-normality a linear time integration of the Navier-Stokes equations (1) is performed. A divergence-free, random uniformly distributed perturbation is added at  $t = 0$  to the azimuthal component  $U_{b\theta}$  of the base flow. The equations linearized around the base flow are then advanced in time. Rather than focusing on the traditional energy gain as in Ref. [8], here we monitor in time the  $L_2$  norm of the azimuthal vorticity perturbation

$$a(t) = \|\omega_{\text{pert}}\| = \sqrt{\int |\omega - \omega_b|^2 r dr dz}, \quad (11)$$

where  $\omega = \partial_z u_r - \partial_r u_z$  is the azimuthal vorticity component,  $\omega_b$  the equivalent quantity for the base flow and  $\omega_{\text{pert}}$  the difference between the two, whose square is plotted in Fig. 5.

The time evolution of  $a(t)$  resulting from linearized and nonlinear time integrations are compared in Fig. 5. Initially almost identical, these signals diverge when the nonlinear code starts to approach the large amplitude solution branch, a snapshot of which has already been shown in Fig. 2. The observable  $a^2$ , initially around  $10^{-10}$ , is amplified by more than twelve orders of magnitude in less than 20 time units, before it starts to decrease. A growth in energy of this order was also reported in [8]. High levels of non-normal growth are expected to lead to additional difficulties in the present analysis. In particular it makes it impossible to use only a time integrator to capture the base flow and one has to resort to the Newton solver instead. With a time integrator, in the subcritical regime, despite the formal property of linear stability of the base flow, a small perturbation resulting from a very small increment in  $\text{Re}$  will be strongly amplified and will, *in practice*, lead to the chaotic attractor.

For  $\text{Re} = 2900$  which is below  $\text{Re}_c$ , linear stability predicts a negative growth rate. This is visible here in Fig. 5(a) in the asymptotic exponential decay. The quantitative negative growth rate  $\lambda = -3.58 \times 10^{-3}$  matches well the final exponential decay (multiplied by two since  $a^2$  is considered rather than  $a$ ). For  $\text{Re} = 3000$  which exceeds  $\text{Re}_c$ , the decrease of  $a^2$  is followed by an exponentially increase. The exponential growth associated with the most unstable eigenvalue  $\lambda = 1.18 \times 10^{-2}$ , for the corresponding  $\text{Re}$ , is plotted in Fig. 5(b). The good agreement at late times confirms the prediction from linear stability analysis.



#### IV. PERIODIC SOLUTIONS

Finding the critical Reynolds number  $Re_c$  associated with the first destabilization of the laminar base flow is the starting point in the construction of a bifurcation diagram. The rest of the article is devoted to a more complete description of this bifurcation diagram. Since the loss of stability at  $Re = Re_c$  is due to a pair of complex conjugate eigenvalues, it corresponds to a Hopf bifurcation, from which a nonlinear branch of oscillatory solutions is expected to arise. If the branch bifurcates towards  $Re < Re_c$  and features unstable periodic orbits in the neighborhood of  $Re_c$ , the bifurcation is said to be subcritical. If it bifurcates towards  $Re > Re_c$  and features stable limit cycles in the neighborhood of  $Re_c$ , it is said to be supercritical. The periodic solutions can then be continued further in parameter space using arclength continuation.

In order to identify oscillatory solutions near a Hopf bifurcation point, the recent self-consistent method (SCM) [24] will be used. It was previously used with success for the supercritical bifurcation of the two-dimensional wake behind a circular cylinder [24]. A quick summary of the method is presented in Sec. IV A.

An *a priori* reasonable expectation, given the sustained subcritical states observed in Ref. [8], is that a Hopf branch of unstable solutions bifurcates subcritically directly from the base flow at  $Re = Re_c$ . Such a branch could ideally be continued down to low values of  $Re$ , before it folds back and bifurcates into new solutions that form the backbone of the chaotic attractor (as in, e.g., Ref. [29]). This expectation will be confronted with the present results in Sec. IV C. In the quest for the Hopf branch using SCM, another branch of periodic solutions was unexpectedly found, which will be reported in Sec. IV D. As will be shown, unlike the Hopf branch which appears in fact supercritical, this new branch is subcritical and does extend to low  $Re$  values.

##### A. Self-Consistent Method (SCM)

The SCM serves as an algorithmic tool to find the periodic solutions of the system (1) near a Hopf bifurcation point. It assumes that the periodic solution can be described as a sum of a steady field  $\mathbf{U}$  (the *mean flow*, which is generally distinct from the base flow) and an oscillatory field of complex amplitude  $\mathbf{u}'$  together with its complex conjugate  $\mathbf{u}'^*$  (the *oscillatory mode*). Denoting  $\mathbf{U}$  the mean velocity field and  $P$  the mean pressure field, the following ansatz is considered with  $\lambda$  a complex number ( $\lambda = \lambda_r + i\lambda_i$ ) and  $\lambda^*$  its conjugate:

$$\mathbf{u} = \mathbf{U} + A(\mathbf{u}'e^{\lambda t} + \mathbf{u}'^*e^{\lambda^* t}), \quad (12a)$$

$$p = P + A(p'e^{\lambda t} + p'^*e^{\lambda^* t}). \quad (12b)$$

The additional real parameter  $A$  is introduced to cope with the fact that  $\mathbf{u}'$  is defined up to a multiplicative constant. The ansatz (12) is introduced into the Navier-Stokes equation (1). Separating the steady and oscillatory parts, and retaining only the terms oscillating at angular frequency  $\pm\lambda_i$ , the resulting set of equations is

$$(\mathbf{U} \cdot \nabla)\mathbf{U} + 2A^2(\mathbf{u}'^* \cdot \nabla)\mathbf{u}' = -\nabla P + \frac{1}{Re}\nabla^2\mathbf{U}, \quad \nabla \cdot \mathbf{U} = 0, \quad (13a)$$

$$\lambda\mathbf{u}' + (\mathbf{u}' \cdot \nabla)\mathbf{U} + (\mathbf{U} \cdot \nabla)\mathbf{u}' = -\nabla p' + \frac{1}{Re}\nabla^2\mathbf{u}', \quad \nabla \cdot \mathbf{u}' = 0. \quad (13b)$$

Equation (13a) forms a forced nonlinear steady Navier-Stokes equation for the field  $\mathbf{U}$  with a forcing term proportional to  $(\mathbf{u}'^* \cdot \nabla)\mathbf{u}'$ . Equation (13b) results from the formal linearization of the Navier-Stokes equations around the mean flow  $\mathbf{U}$ . This amounts to neglecting all  $o(A)$  terms (which is consistent with discarding terms that oscillate at  $2\lambda_i$ ) even if in practice we will consider  $A = O(1)$ . Equation (13b) is an eigenvalue problem of the same form as Eq. (9) except that  $\mathbf{U}_b$  is replaced by  $\mathbf{U}$ . The associated eigenvector  $\mathbf{q}' = (u'_r, u'_\theta, u'_z, p')$ , computed using ARPACK, is normalized to unit amplitude with respect to the  $\mathbf{B}$  matrix (10) such that  $\mathbf{q}'^*\mathbf{B}\mathbf{q}' = 1$ . By starting from suitable guesses for  $\mathbf{U}$  and  $\mathbf{u}'$  for a given parameter  $A$ , an iterative method is used to solve the

two equations (13a) and (13b) alternately until convergence. The next value for  $A$  is then sought for iteratively using a secant method until the steady state  $\mathbf{U}$  becomes neutrally stable, i.e.,  $\lambda_r = 0$ . We emphasize that SCM operates according to two loops, an inner and an outer one. In the inner loop Eqs. (13a) and (13b) are solved alternately, for fixed  $A$ , with the result of one equation feeding the other one until convergence. In the outer loop the parameter  $A$  is changed using a secant method until  $\lambda_r = 0$ . The whole procedure results in the oscillatory solution described by Eqs. (12a) and (12b). More details on the method can be found in Ref. [30].

### B. Harmonic Balance Method (HBM)

The Newton method discussed in Sec. II C was used to identify steady-state solutions. It can be generalized for the identification of periodic orbits. While the use of a Newton method for steady states is standard procedure, its generalization to periodic orbits has only been used recently in fluid dynamics and is thus explained in more detail here. Exactly periodic solutions can be approximated by a finite Fourier expansion of the form

$$\mathbf{u}(\mathbf{x}, t) = \mathbf{U}(\mathbf{x}) + \sum_{k=1}^{nt} \{ \mathbf{u}_k(\mathbf{x}) e^{ik\omega t} + \mathbf{u}_k^*(\mathbf{x}) e^{-ik\omega t} \}, \quad (14a)$$

$$p(\mathbf{x}, t) = P(\mathbf{x}) + \sum_{k=1}^{nt} \{ p_k(\mathbf{x}) e^{ik\omega t} + p_k^*(\mathbf{x}) e^{-ik\omega t} \}, \quad (14b)$$

where  $\omega$  is a (real) angular frequency,  $nt$  is a finite positive integer, and the asterisk stands again for complex conjugate. The identification of periodic orbits based on this truncated Fourier expansion is sometimes described as the harmonic balance method in the literature, which was recently used in different flow cases [25,26]. The value of  $nt$  parametrizes the accuracy of the spectral approximation, with convergence guaranteed for increasing  $nt$  provided the time dependence is smooth enough. When the periodic orbit is simple enough, for instance close to a bifurcation point, a small number of harmonics may be enough to describe it accurately, whereas for more complex periodic dynamics more harmonics will be required.

Once the finite Fourier decomposition (14) is introduced into the Navier-Stokes equation (1) as an ansatz for  $\mathbf{u}$  and  $p$ , a set of nonlinear equations arises: one equation for each of the steady fields  $\mathbf{U}$ ,  $P$  and the others for each Fourier component  $\mathbf{u}_k$ ,  $p_k$  with  $1 \leq k \leq nt$ . This set of nonlinear equations can be solved using a Newton method to determine the fields  $\mathbf{U}$ ,  $P$ ,  $\mathbf{u}_k$ ,  $p_k$  for all  $k$  and the unknown angular frequency  $\omega$ . A temporal phase condition is added to the list of equations to make the Newton system well posed. Indeed, the orbit is defined up to a phase shift. Different types of phase conditions can be imposed. For example, a value or a derivative of a variable is fixed at a specific point along the orbit. Imposing a derivative to zero for an arbitrary variable is generally a good choice and avoids requiring the knowledge of a specific value. Other phase conditions, less straightforward to implement, such as an integral phase condition can be imposed and is often favored when solving ordinary differential equations (see chapter 7 of [31]). Here, as a phase condition, the time derivative of the radial velocity is fixed to zero at the beginning of the orbit and at one point in the domain. The Newton algorithm is converged to machine precision (i.e., when the Euclidean norm of the residual vector of the Newton method drops to  $10^{-11}$  or less). Importantly, the decomposition (14) for  $nt = 1$  is the decomposition used in the original SCM in Ref. [24] at convergence. Thus, SCM and HBM for  $nt = 1$  differ only in the iterative process of convergence of the solution. Once one solution of the Navier-Stokes equations is converged using HBM it can be continued in parameter space using standard arclength continuation [32].

### C. Hopf branch

The branch of oscillatory solutions bifurcating at  $Re_c$  is labeled the Hopf branch. Solutions on this branch are assumed exactly periodic, i.e., of the form (14). When using only one oscillatory mode this form reduces to (12). The coupled problem (13a)–(13b) is first solved for  $A = 0$  and then

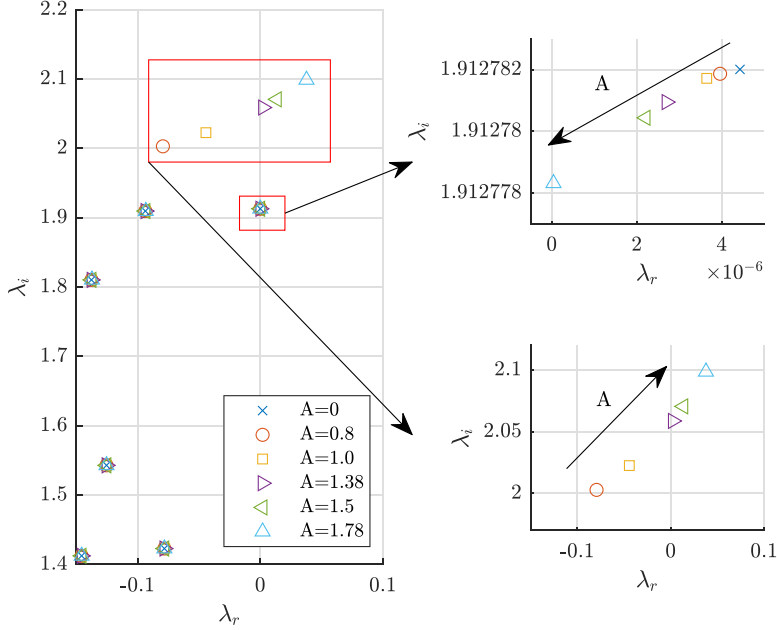


FIG. 6. Application of self-consistent method (SCM) following Eq. (13). Spectrum evolution for  $\text{Re} = 2925.5 \gtrsim \text{Re}_c = 2925.47$  with changing amplitude  $A$  of the forcing. When no forcing is applied ( $A = 0$ ) the base flow is unstable to a single eigenvector with the corresponding eigenvalue  $\lambda = 4.4 \times 10^{-6} + 1.912782i$  (blue cross in inset). Top right inset: eigenvalue evolution of the eigenvalue  $\lambda$  leading to the Hopf branch discussed in Sec. IV C. Each symbol marks the convergence of an inner loop process. The outer loop starts at  $A = 0$  and converges for  $A \approx 1.78$ , when the resulting eigenvalue has a zero real part (only a few selected values of  $A$  are shown here). Bottom right inset: evolution of another eigenvalue eventually leading to the discovery of another branch as described in Sec. IV D. Spatial resolution R0.

for  $A = 0.8$  ( $\text{Re} = 2925.5 > \text{Re}_c = 2925.47$ ). The vector  $\mathbf{u}'$  in the forcing terms (13a) is selected in both cases as the most unstable eigenvector from Eq. (13b). Comparing the converged spectra for  $A = 0$  and  $A = 0.8$ , the most unstable eigenvalue has moved towards the left upon increasing  $A$  (see Fig. 6). Therefore, a value of  $A = A^*$  such that  $\mathbf{U}$  becomes neutrally stable, i.e.,  $\lambda_r = 0$ , presumably exists nearby. This value  $A^*$  is sought using the secant method. For the spatial resolution R0 this value is  $A^* \approx 1.78$ , as shown in Fig. 6. This controlled SCM procedure has proven essential in catching the Hopf branch. The basin of attraction is small, hence for a given  $\text{Re} > \text{Re}_c$ , the amplitude  $A$  must be very close to  $A^*$  so as not to diverge.

Finding the neutrally stable field  $\mathbf{U}$  and the corresponding oscillatory field  $\mathbf{u}'$  yields one solution on the Hopf branch. Continuation in parameter space allows one to progress along the branch, which is displayed in Fig. 7 using the time-average scalar observable  $a$  defined by (11).

The analysis of the Hopf branch leads to a few specific observations:

- (i) A branch of periodic solutions is born at  $\text{Re}_c$  as expected
- (ii) at its onset the branch bifurcates towards  $\text{Re} > \text{Re}_c$
- (iii) the amplitude of the oscillating solution scales like  $\sqrt{\text{Re} - \text{Re}_c}$  near the bifurcation point.

The Hopf bifurcation occurring at  $\text{Re} = \text{Re}_c$  is therefore supercritical, at odds with earlier expectations. While the approximation  $nt = 1$  is valid close enough to  $\text{Re}_c$ , at a finite distance from it more temporal Fourier modes are needed, corresponding to  $nt > 1$ . A few observations can be made:

- (i) The solutions for  $nt = 1, 2$  and 3 collapse onto each other near  $\text{Re}_c$  but only in the very narrow range  $0 < \text{Re} - \text{Re}_c < 10^{-4}$ . This means that the strong assumption of the simple form of the limit cycle is valid only very close to  $\text{Re}_c$  for this flow.

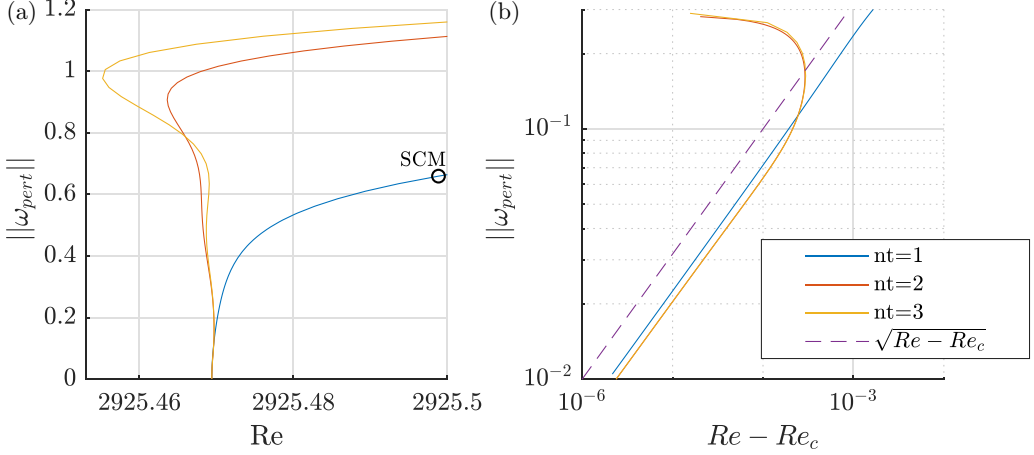


FIG. 7. (a) Onset of the Hopf branch for increasing parameter  $nt$ . The point at which the initialization from the SCM solution to HBM solution is done is marked with a black circle. (b) Zoom on the region  $10^{-6} < Re - Re_c < 10^{-3}$  with  $Re_c = 2925.47$ , where the supercritical scaling  $a \propto \sqrt{Re - Re_c}$  (dashed line) holds (logarithmic scale). The color scheme is the same for both plots. Spatial resolution R0.

(ii) The  $nt = 2$  and  $nt = 3$  solutions collapse onto one another longer but diverge from one another when  $||\omega_{pert}|| \approx 0.5$ . This means that the solutions on the Hopf branch becomes increasingly complicated away from  $Re_c$ . Generally, whenever the branches for subsequent  $nt$  stop overlapping they are considered temporally unresolved, and special care should be taken when interpreting the results.

(iii) The Hopf branch shoots up vertically from the bifurcation point. On one hand any approximation error introduced by a finite difference scheme in time would move  $Re_c$  and the branch in parameter space, on the other hand the vanishing growth rates imply large integration times. This explains why they were not identified in Ref. [8]. Besides the strong non-normality of the linearized dynamics around the base flow (see Sec. III B) carries over to the Hopf branch. The solutions on the Hopf branch are therefore believed to be virtually intractable using a time integrator. The link between strong non-normality and the steepness of the Hopf branch near criticality is discussed for instance in [33].

The whole SCM initialization and HBM continuation procedure were repeated for the spatial resolution R2. The result appears to be qualitatively mesh-independent (not shown) and the finding of the bifurcation being supercritical is therefore robust. Recalling the expectation that a subcritical bifurcation at  $Re_c$  could explain the occurrence of concentric rolls at low enough  $Re \ll Re_c$ , the results can appear so far as disappointing. Not only is the Hopf branch supercritical, but the several folds that occur along the branch keep this branch limited to a relatively narrow  $O(1)$  range in  $Re$ . Although further continuation past many folds could shed more light on this question, it appears safe to claim that the Hopf branch close to  $Re_c$  is probably not likely to explain the subcritical sustained states reported here and in [8] at  $Re \approx 2000$ .

Interestingly, for  $A = 1.38$  another eigenvalue, characterized by  $\lambda_i > 2$ , is close to becoming neutrally stable (see the purple triangle in the leftmost part of Fig. 6). This means that, provided the eigenvector of the forcing in the equations (13) is changed to that eigenvector, SCM can again be used as an initial guess to uncover another branch of periodic solutions. This process is described in the following section.

#### D. Periodic-subcritical branch

We describe here how a another branch of periodic solutions, different from the Hopf branch, was identified numerically as a by-product of the search for the Hopf branch. As the choice of

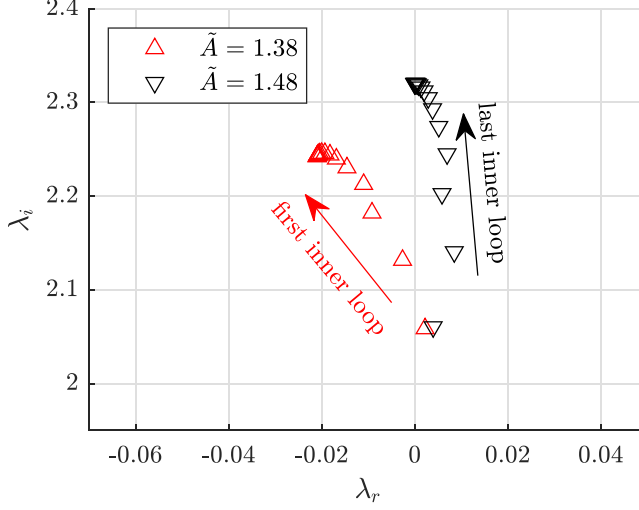


FIG. 8. Determination of the periodic-subcritical branch using SCM. At  $A = 1.38$  the eigenvector  $\mathbf{u}'$  was changed to another eigenvector  $\tilde{\mathbf{u}}'$  (see text) with an amplitude denoted as  $\tilde{A}$ .  $\tilde{A}$  is set to 1.38 for the first inner loop. The red triangles show the convergence of the inner loop for  $\tilde{A} = 1.38$  with the final  $\lambda_r \neq 0$ . After achieving convergence on  $\tilde{A}$  the last inner loop is shown using black triangles for  $\tilde{A} = 1.48$  with the final  $\lambda_r \approx 0$  and corresponding  $\lambda_i \approx 2.33$ . This convergence process on  $\tilde{A}$  takes approximately 10 iterations. For the sake of clarity only the first and the last inner loops are shown.

the eigenvector  $\mathbf{u}'$  (resp.  $\mathbf{u}'^*$ ) used in Eq. (13a) is after all arbitrary, it can be traded for any other eigensolution  $\tilde{\mathbf{u}}'$  (resp.  $\tilde{\mathbf{u}}'^*$ ) of Eq. (13b).  $\tilde{\mathbf{u}}'$  is associated with an eigenvalue of imaginary part  $\lambda_i \approx 2.05$  rather than the previous eigenvalue  $\lambda_i \approx 1.91$ . The substitution  $\mathbf{u}' \leftarrow \tilde{\mathbf{u}}'$  was performed at the end of the outer iteration that resulted in  $A = 1.38$ . The eigenvector  $\tilde{\mathbf{u}}'$  chosen, associated with an amplitude denoted  $\tilde{A}$ , was indeed close to neutral during the resolution of Eq. (13a) with  $A = 1.38$  (see Fig. 6), which makes it an alternative interesting guess for SCM. After the substitution, the

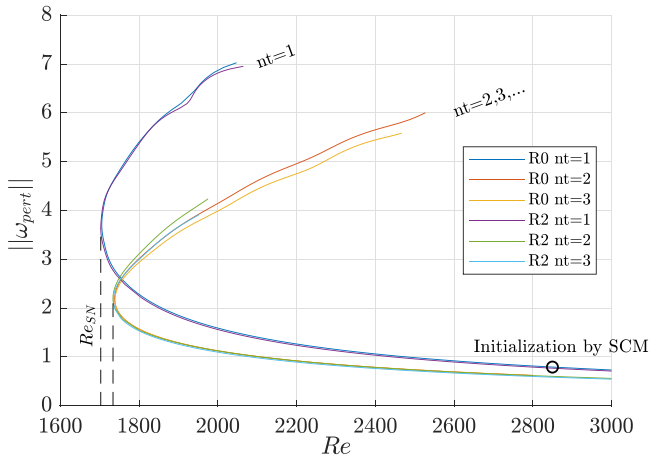


FIG. 9. Periodic-subcritical branch for discretizations R0 and R2 and increasing  $nt$ , where  $nt$  is the number of Fourier modes in the decomposition (14). The point at which the initialization from the SCM solution to HBM solution is done is marked with a black circle. Branches fold around  $Re = Re_{SN} \approx 1700$ . The exact saddle-node bifurcation values are listed in Table II.

TABLE II. Saddle-node value  $\text{Re}_{SN}$  depending on the spatial and temporal discretization.

$nt$	1	2	3
R0	1705.3	1738.1	1738.9
R2	1702.8	1733.9	1734.7

mean flow is no longer neutrally stable, but the SCM inner and outer iterations can resume. During this second process we observe a substantial increase in  $\lambda_i$  from  $\approx 2.05$  to  $\approx 2.3$ . At convergence the new amplitude  $\tilde{A} \approx 1.48$ . The first and the last step of the secant method (the outer loop) are illustrated in Fig. 8. When SCM is sufficiently converged, the solution is used to initialize HBM. HBM is used to converge the solution, which is then continued in parameter space (see Fig. 9).

The above methodology yields a branch very different from the Hopf branch. This branch extends down to  $\text{Re} \approx 1700$ , i.e., much lower than both  $\text{Re}_c$  and the Hopf branch altogether. The newly found branch is hence called the *periodic-subcritical branch*. Precise values of  $\text{Re}$  at which this saddle-node bifurcation happens,  $\text{Re}_{SN}$ , are documented in Table II. Its lower part also extends towards values of  $\text{Re} \gg \text{Re}_c$ , at least up to 7000 for both grid resolutions (not shown). This branch was therefore *not* found to bifurcate from the steady state in the range of  $\text{Re}$  investigated. The angular frequencies of the solutions on this branch are reported in Table III.

Since the periodic-subcritical branch exists over a wider range of  $\text{Re}$  values than the Hopf branch, the corresponding solutions are studied in more detail. In particular a solution from the lower branch is visualized in Fig. 10 for  $\text{Re} = 2300$ . It takes the form of rolls in the Bödewadt layer visually comparable to the most unstable eigenvector for the  $\text{Re} \approx \text{Re}_c$ . The decomposition in Eqs. (14), used in the Newton method, allows for a direct analysis of the temporal harmonics of this solution. Subsequent oscillation modes are characterized by increasingly smaller structures. Any improvement in the temporal resolution  $nt$  must hence be accompanied by an increase in spatial resolution ( $N_r \times N_z$ ).

## V. EDGE STATES

In this section we focus on another type of finite-amplitude solution likely to contribute to the bifurcation diagram of the system. The third branch of solutions reported in the present work is a branch of *edge states*. As we shall see, their dynamics is more complex than that of the periodic states of Sec. IV. They are known to play a major role as mediators between the base flow and the chaotic state [34], here the chaotic rolls.

### A. Notion of edge state

Edge states are unstable finite-amplitude states, generally associated with low levels of perturbation energy, that are specific to the subcritical regime where the base flow is linearly stable. They have the defining property that their instability leads both to the chaotic solutions or to the base

TABLE III. Angular frequency of the periodic solutions on the periodic-subcritical branch shown in Fig. 9. The point corresponding to the saddle node bifurcation is emphasized in bold.  $\text{Re}$  to the left (right) of this point correspond to the top (bottom) part of the periodic-subcritical branch in Fig. 9.  $\omega_{\text{per-sub}}$  corresponds directly to the angular frequency used in formula (14). Resolution R2,  $nt = 3$ .

$\text{Re}$	1900	1800	<b>1734.7</b>	2000	2300	2600	3000
$\omega_{\text{per-sub}}$	3.934	3.586	<b>3.136</b>	2.559	2.421	2.351	2.297
$f$	0.626	0.570	<b>0.499</b>	0.407	0.385	0.374	0.365



FIG. 10. (a) Contours of  $U_\theta$ . (b)–(d)  $u_\theta$  for temporal harmonics  $k = 1, 2, 3$  (from top to bottom) for the lower periodic-subcritical solution at  $\text{Re} = 2300$ . Spatial resolution  $R0$ ,  $nt = 3$ .

flow, depending on the perturbation considered [35]. Mathematically, in the state space associated with Eq. (1), edge states are local attractors belonging to the intersection of the respective attraction basins of attraction of the base flow and of the chaotic set. They exist as soon as the base flow has a nontrivial basin of attraction, i.e., in subcritical conditions, here for  $\text{Re} < \text{Re}_c$ . The intersection of the boundaries of these basins of attraction is the stable manifold of the edge state, sometimes called simply the *edge*. The first computation of edge tracking in fluid flows is due to [36] in channel flow. Later computations have shown that edge states are generally spatially localized structures [34,37]. Importantly, the dynamical nature of an edge state is not known in advance, it can be a steady state, a periodic orbit, or a more complicated object such as a chaotic set [38–40]. More details on the concept of edge state can be found in [35,37,39,41,42]. The technique is particularly useful when combined with symmetry subspace restrictions [39,43]. The aim of this section is to report, for the first time in the literature, calculations of edge states in rotor-stator flow for a set of Reynolds numbers.

### B. Bisection algorithm

Following the above definition, the main idea behind the bisection algorithm is to find two points bracketing the stable manifold sufficiently close, such that the associated trajectories approach transiently the edge state. Starting with two flow states, one labeled *turbulent* and the other *laminar*, a new initial condition is formed using the interpolation

$$\mathbf{u}(t=0) = (1 - \alpha)\mathbf{u}_{\text{laminar}} + \alpha\mathbf{u}_{\text{turbulent}}, \quad 0 < \alpha < 1. \quad (15)$$

This linear combination of the laminar state  $\mathbf{u}_{\text{laminar}}$  and a turbulent state  $\mathbf{u}_{\text{turbulent}}$  is the new initial condition for time integration. Depending on whether this new initial condition evolves towards the turbulent or laminar state, the initial condition is labeled as turbulent or laminar for the next iteration. This yields a sequence of  $\alpha$  values  $\alpha_0, \alpha_1, \dots$ . The process is repeated until the sequence of  $\alpha_i$ s has converged. After each iteration the bracketing interval is halved, therefore the value of  $\alpha$  for which the simulation shadows the edge the longest is determined up to machine precision (taken



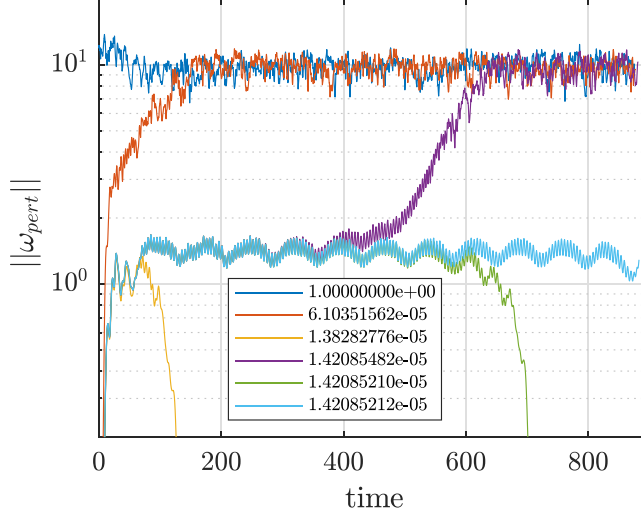


FIG. 11. Time series of the observable  $a(t)$  during the bisection procedure for . Legend: coefficient  $\alpha$  [defined in Eq. (11)] parametrizing the initial condition. Spatial resolution R0.

to be  $10^{-16} \approx 2^{-53}$ ) after approximately  $|\log(10^{-16})/\log 2| \approx 53$  iterations. This apparent limitation of the bisection algorithm by finite machine precision can be easily overcome by a *restart procedure* [35]. By restarting the bisection from a later time it can run indefinitely and the edge state is reached asymptotically.

The same observable  $a(t)$  defined in Eq. (11) is used to monitor edge trajectories and the bracketing trajectories. If  $a(t \rightarrow \infty) = 0$  the trajectory has reached the laminar base flow.

### C. Edge branch

The bisection procedure is now used to identify edge states in the rotor-stator flow. The time history of the observable  $a(t)$ , the vorticity perturbation norm, is reported for  $Re = 2300 < Re_c$  in Fig. 11. Some guiding values of the interpolation coefficient  $\alpha$  are provided in the legend. Bisection successfully identifies a state that is unstable and lies, by definition, at the boundary of the basins of attraction of the chaotic and the laminar regime. The same bisection procedure is repeated from  $Re \approx Re_c$  down to where bisection fails due to the apparent lack of chaotic attractor. A representative portion of the corresponding time series is displayed in Fig. 12. The signal on the edge seems chaotic for  $Re = 1850$ , almost periodic for  $Re = 2000$  and apparently biperiodic for  $Re > 2300$ . We observe that the bisection algorithm detects also the unstable solution at  $Re = 3000$  which is only a few percent above  $Re_c = 2925.47$ . Since  $Re > Re_c$  this state is not formally an edge state because

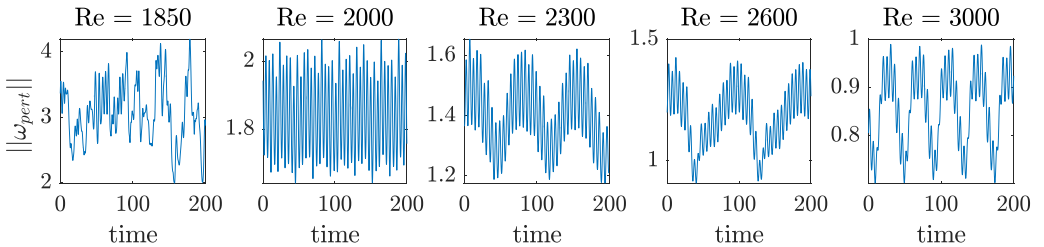


FIG. 12. Perturbation vorticity signal  $a(t)$  corresponding to the edge state, for the same values of  $Re$ . From left to right,  $Re = 1850, 2000, 2300, 2600$ , and  $3000 > Re_c$ .

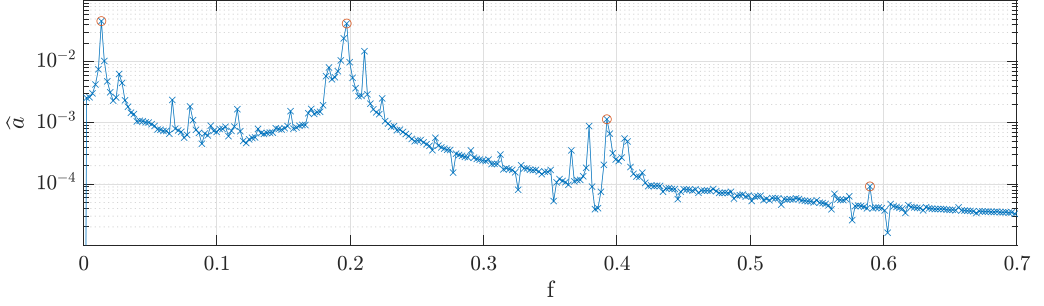


FIG. 13. Frequency spectrum  $\hat{a}(f)$  of the observable  $a$ . Spatial resolution R0. The spectrum is calculated using 2043 samples of the signal sampled uniformly in the time interval  $t \in (300, 750)$ . The maximum frequency computed is  $f_{\max} = 2.27$  with a frequency step  $df = 0.0022$ . The frequencies marked with red dots are listed in Table IV.

the laminar basin has collapsed to a single point. As demonstrated in Ref. [44] using a low-order model, the edge state can still exist as finite-amplitude solution of Eq. (1) beyond  $Re_c$  although it loses its property of state space mediator. This collapse of the edge state makes it however, in principle, undetectable by standard bisection. Here the reason is simpler and due to the finite time over which the edge has been followed. Since the base state at  $Re = 3000$  is only slightly unstable, it takes much more time for the unstable perturbation to the base flow to grow than it takes for the perturbation to the unstable edge state to grow. This explains why the bisection algorithm still detects an unstable solution near  $Re_c$  even for  $Re \gtrsim Re_c$ . The edge state found at  $Re = 2300$  is chosen for further analysis because of its simple dynamics and its apparent biperiodicity, an original property reported only lately in Refs. [43,45] in the context of lid-driven cavities.

#### D. Frequency analysis

A first glance at the observable time series for  $Re = 2300$  suggests the presence of two main frequencies in the edge state: one corresponding to the long period  $T \approx 75$ , and one corresponding to a shorter period  $T \approx 5$ . For a first identification of the interesting frequencies the Fourier transformed of the *global* observable  $a(t)$  is used. It is preferred to the velocity signal from a *local* probe because, as a global quantity, it gives an overview of *all* frequencies contributing to the edge state. A part of the signal corresponding to the final bisection iteration seen in Fig. 11 is extracted and its frequency spectrum is computed. Care has been taken to disregard the initial and final transients of the signal. The remaining time interval available for the Fourier transform contains only approximately six long periods, hence finite-time effects should be expected to pollute the subsequent analysis. The frequency spectrum  $\hat{a}(f)$  is plotted in Fig. 13 as a function of the frequency  $f$ . A number of distinct discrete peaks can be observed. The frequencies marked with red circles are listed in increasing order in Table IV. The slow frequency ( $f = 0.013$ ) in the spectrum corresponds to the long period seen in the observable signal ( $T \approx 75$ ). A series of peaks corresponding to  $f = 0.197, 0.392, 0.590$  correspond to the fast oscillations of  $a$ .

Further insight is gained by computing the Fourier transform of the (discrete) velocity field itself. For this purpose a series of flow fields is saved. A snapshot of the associated perturbation

TABLE IV. Frequencies and periods of the main peaks from the frequency spectrum  $\hat{a}(f)$  in Fig. 13.

Frequency	0.013	0.197	0.392	0.590
Period	75.175	5.068	2.548	1.695

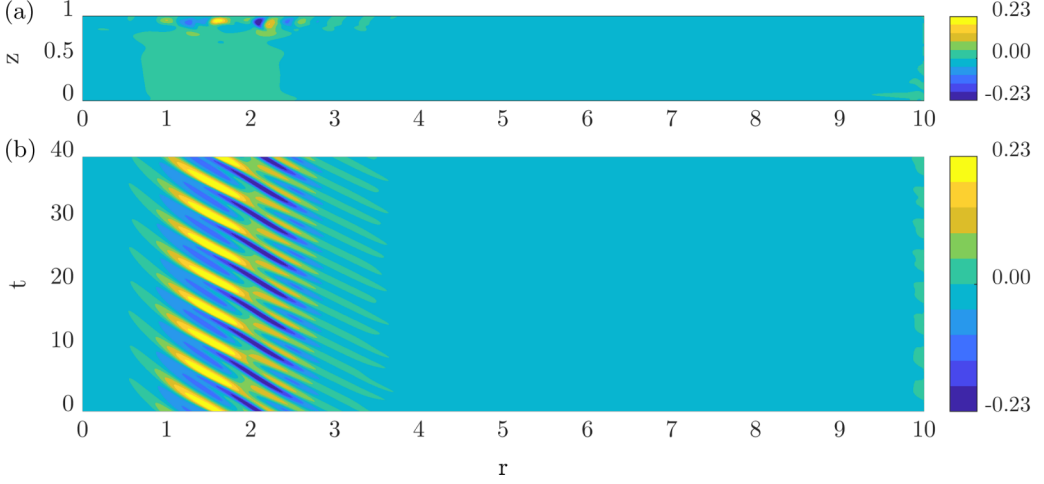


FIG. 14. (a) Edge state snapshot of  $u_\theta(r, z)$  in perturbation mode. (b)  $(r, t)$  space-time diagram of  $u_\theta(r, z)$  at  $z = 0.9375$  (bottom) for  $\text{Re} = 2300$ . Rolls are localized in the Bödewadt layer and travel towards the axis. Spatial resolution R0. A video that shows the temporal evolution of  $u_r$  and  $u_\theta$  in the meridional plane, during the instability of the edge state, is available as Supplemental Material (see the first half of the movie) [48].

velocity is shown in Fig. 14 together with a space-time diagram. The space-time diagram shows clearly the pairing and merging of the vortical structures as they propagate towards the axis inside the envelope (between  $r = 1$  and  $r \approx 3.5$ ). Interestingly, whereas we are now describing an edge state which by definition is unstable, the same pairing phenomenon has also been reported, for a smaller aspect ratio, as a feature of the propagation of the rolls observable experimentally [5]. A Fourier transform is computed at each point of the (discretized) domain using 2043 snapshots sampled uniformly over the time interval  $t \in (0, 450)$ . After bandpass filters around frequencies  $f = 0.013, 0.197, 0.392$ , and  $0.590$  are applied, the velocity field corresponding to each frequency is reconstructed in physical space. The azimuthal velocity components associated with each frequency are shown in Fig. 15.

The velocity fields corresponding to higher frequencies [ $f = 0.197, 0.392$ , and  $0.590$ , Figs. 15(b)–15(d)] feature a wavetrain of counter-rotating vortices located inside the Bödewadt layer. These waves have negative radial phase velocity, i.e., they propagate in the direction of decreasing radius, as is clear from the spacetime diagram in Fig. 16 (bottom). Interestingly, the waveform corresponding to  $f = 0.392$  bears a high resemblance to the  $k = 1$  mode of the periodic subcritical solution reported in Sec. IV D, particularly in Fig. 10. For  $\text{Re} = 2300$ , the frequency of the periodic subcritical solution is  $f_{\text{per-sub}} = 0.3854$ , whereas the corresponding frequency for the edge state is  $f_{\text{FT}} = 0.3924$ .

The Fourier mode at the slow frequency [ $f = 0.013$ , Fig. 15(a)] features vortical structures at the edge of the Bödewadt layer for  $r \in (1, 3)$  and  $z \in (0.8, 1)$ . Using a space-time diagram computed for  $z = 0.5$ , an apparent wavepacket of nearly vanishing radial group and phase velocity is prominent for  $r \in (1, 3)$  and  $z \in (0, 0.8)$ ; see Fig. 16(a). Vertical structures exist also outside the Bödewadt layer. Consistently with the dispersion relation of inertial waves in flows with solid body rotation, such structures can be interpreted as low-frequency inertial waves. These slow waves, interpreted as spatially localized standing waves (with vanishing phase velocity), are also reminiscent of the internal waves observed inside the bulk of differentially heated cavities [46, 47].

As a yet stronger sign that the periodic and the edge solutions are connected, the Fourier mode extracted from the edge state corresponding to  $f = 0.392$  is used as an initial guess for HBM with  $nt = 2$ . This is achieved in practice by building an initial guess for Newton's with  $(\mathbf{U}, P)$  as the mean solution, the edge mode corresponding to  $f = 0.392$  as the first Fourier mode and the corresponding

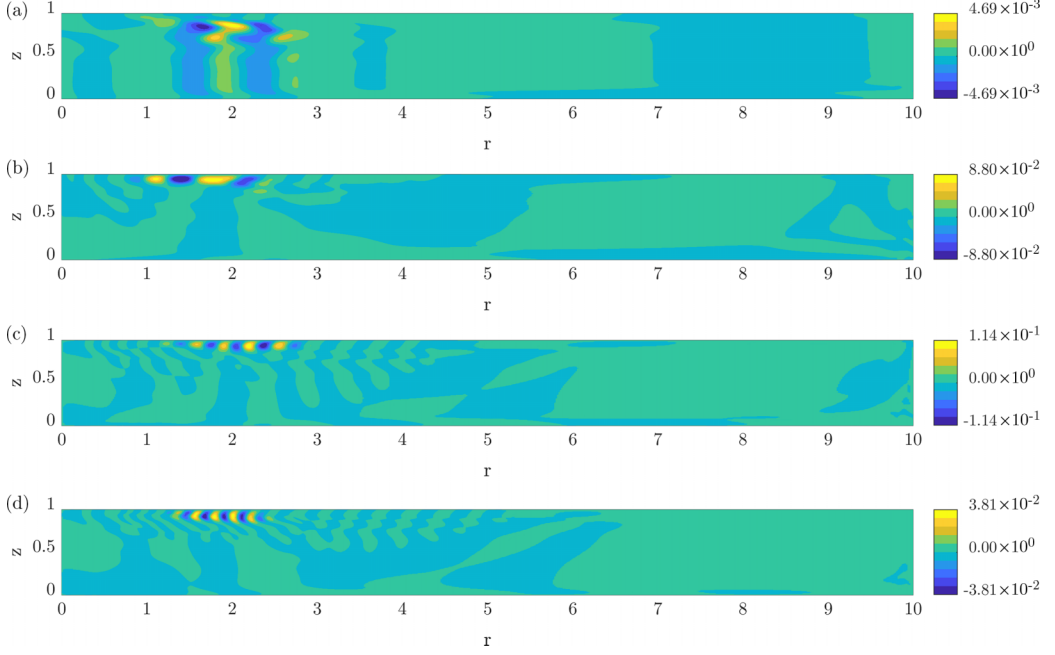


FIG. 15. Temporal Fourier components of the edge state corresponding to frequencies (a)  $f = 0.013$ , (b)  $f = 0.197$ , (c)  $f = 0.392$ , and (d)  $f = 0.590$ , as shown in the spectrum in Fig. 13. An associated movie available in the Supplemental Material [48]. Note the resemblance between panel (c) and the  $k = 1$  harmonic in Fig. 10.

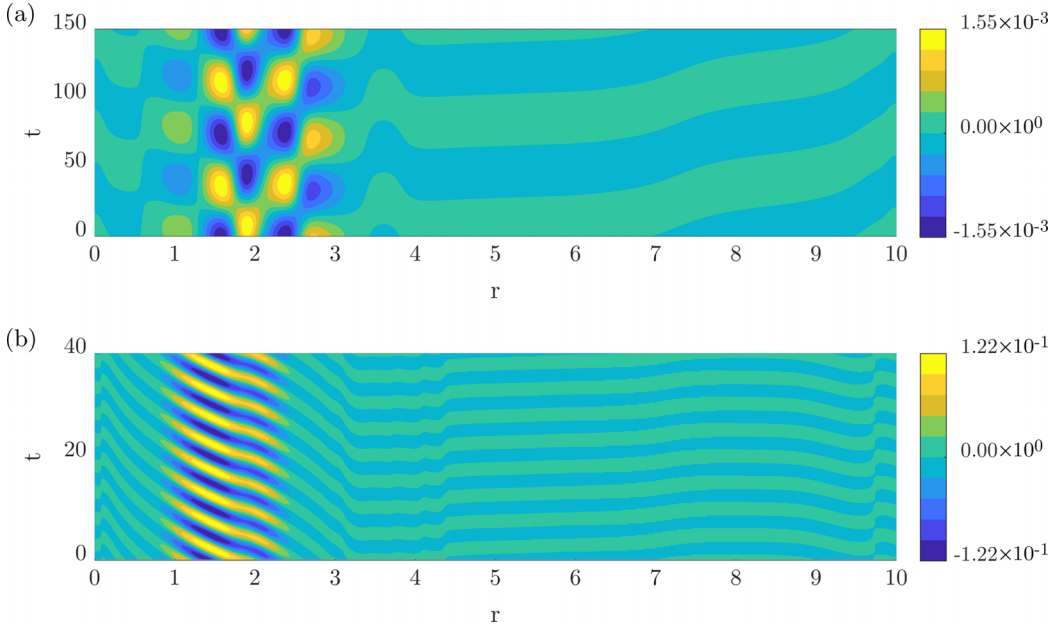


FIG. 16.  $(r, t)$  space-time diagrams of selected temporal Fourier modes for the edge state at  $\text{Re} = 2300$ . Spatial resolution R0. (a) Mode  $f = 0.013$ ,  $z = 0.5$  (midplane cut, compare with Fig. 15(a)); (b) Mode  $f = 0.197$ ,  $z = 0.9375$  (Bödewadt layer cut, as in Fig. 15(b)). The timescale and amplitude scale differ between the two figures.

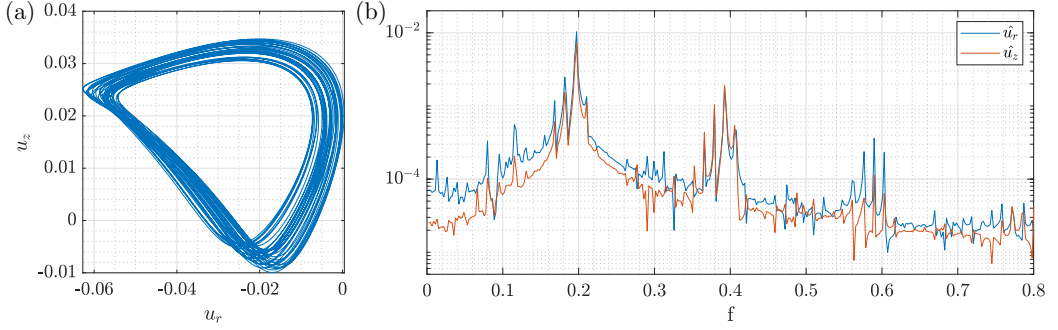


FIG. 17. Velocity data at position  $r = 1.0$ ,  $z = 0.9375$  for the edge state at  $\text{Re} = 2300$ . (a) Phase portrait using in-plane velocities  $u_r$  and  $u_z$  and the spectrum of probe signal. (b) Frequency spectrum computed using  $\approx 100k$  samples spaced uniformly in  $t \in (0, 450)$ . Maximum frequency:  $f_{\max} = 113$  with a resolution  $df = 0.0022$ . Spatial resolution  $R0$ .

angular frequency. Convergence towards the formerly found periodic solution is obtained for  $nt = 2$  in 15 Newton iterations. This indicates that the SCM method was *a posteriori* not the unique way to determine numerically the periodic-subcritical branch. The almost identical frequencies and waveforms suggest that the periodic-subcritical solution found in Sec. IV D is itself an unstable solution embedded in a less unstable edge state. This situation happens to be common when edge states are chaotic [39], but deserves closer inspection here where the edge state is quasiperiodic in time. A simple possibility is that the edge state bifurcates, directly or indirectly, from the subcritical periodic branch. This is left for future investigation.

### E. Quasiperiodicity of the edge state

In order to validate the hypothesis of a quasiperiodic edge state for  $\text{Re} = 2300$ , a velocity probe is considered where the rolls achieve large amplitudes in Fig. 14. A state portrait based on the in-plane velocity components  $u_r$  and  $u_z$  is shown in Fig. 17(a). The plot on the right displays the Fourier transforms of  $u_r(t)$  and  $u_z(t)$ . The Fourier transform displays clear distinct peaks over a nonzero background. It was checked, by artificially shortening the time series, that the background level is not the signature of a chaotic signal, instead it is due to the finiteness of the signal (which is an inherent limitation of the bisection technique). The main peaks correspond to the frequency  $f_1 = 0.197$  and its harmonics, and to  $f_2 = 0.013$  and its harmonics, consistent with the spectrum of  $a(t)$  shown in Fig. 13. The quadratic interplay of these two main frequencies explains the other frequencies  $f = n f_1 \pm m f_2$  with  $(n, m) \in (\mathbb{N} \times \mathbb{N})$  visible in the spectrum. Due to  $f_1$  and  $f_2$  being far apart in the discrete spectrum it is postulated the edge state of the studied rotor-stator flow at the  $\text{Re} = 2300$  is indeed generically biperiodic with two incommensurate frequencies. In other words it forms a 2-torus in the state space of Eq. (1). This property holds in the interval for most values of  $\text{Re}$ . No periodic edge state was identified for the  $\text{Re}$  studied.

### F. Connection between the edge state and the chaotic rolls

By construction, the edge state is a linearly unstable solution of Eq. (1) with a specific property: typical perturbations lead, depending on their sign, either to the laminar base flow or to another chaotic state. We exploit this property and report now the dynamical path from the edge state to the attracting chaotic state [49]. This is achieved simply by selecting and analyzing one of the trajectories displayed in Fig. 11 for  $\text{Re} = 2300$ . A space-time diagram of the azimuthal velocity perturbation along the line  $z = 0.9375$  is shown in Fig. 18. The dynamics follows closely the biperiodic dynamics of the edge state until  $t \approx 400$ . From  $t \approx 400$  to  $t \approx 600$ , the perturbation to the base flow undergoes a rapid exponential growth in both energy and observable  $a$  (see Fig. 11).

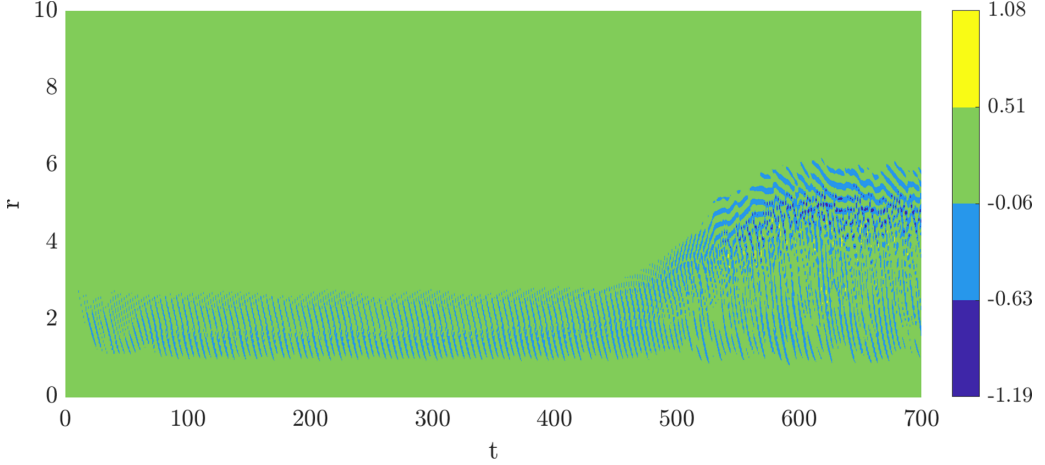


FIG. 18. Instability of the edge state.  $(r, t)$  Space-time diagram for the perturbation  $u_0(r, t)$  at  $z = 0.9375$  for  $\text{Re} = 2300$ . The time series corresponds to one of the *nonconverged* trajectories computed during the bisection process (corresponding to the value  $\alpha = 1.42085482 \times 10^{-5}$ ; see Fig. 11). The departure of the edge state becomes evident for  $t \gtrsim 400$ . The chaotic roll state is reached for  $t \gtrsim 600$ . A movie that shows the temporal evolution of  $u_r$  and  $u_\theta$  in the meridional plane is available as Supplemental Material [48].

For  $t \gtrsim 600$  the stationary chaotic state is reached, with no sign of convergence to any simpler flow state. During the exponential growth phase the radial extent of the edge state grows with time. Whereas the low- $r$  end stays constant to  $\approx 1$ , the large- $r$  of the localized structure moves upstream from  $r \approx 2.5$  to  $r \gtrsim 5$ . This modification results both from an intensification of the perturbations convected away from the corner/shroud region, and from the advection of perturbations *against* the Bödewadt layer (the positive phase speed visible from  $t \approx 500$  to  $t \approx 600$ ). For  $t \gtrsim 520$  the rolls originating upstream of the Bödewadt layer adopt a larger wavelength, a chaotic dynamics with no exact recurrence, and their radial phase speed is reduced (in absolute value) compared to the edge dynamics. Past  $r \approx 4.5$  they decelerate towards the axis with a shorter wavelength and disappear for  $r \leq 1.5$ . The most energetic part of the stationary chaotic regime is found for  $4 < r < 6$  consistently with observations from Fig. 2(c). This is the region where the bulk azimuthal profile departs most dramatically from the self-similar profile, and where ejections from the stator boundary layer occur.

### G. Saddle-node bifurcation and mesh dependence

Figure 19 reports the time average of  $a(t)$  for the solutions lying on the edge, together with the levels corresponding to the chaotic regime. The top (chaotic) branch and the edge branch approach each other for decreasing  $\text{Re}$  and visually suggest that they might connect for  $\text{Re} \approx 1800$ . By analogy with most subcritical shear flows [50], we speculate that the two branches merge in what could abusively be labeled as a saddle-node bifurcation at  $\text{Re} = \text{Re}_{SN} \approx 1800$  (the fact that the top branch is chaotic makes the concept of saddle-node bifurcation somewhat undefined). Interestingly this value of  $\text{Re}_{SN}$  matches approximately the value reported in Table II at which the periodic subcritical branch folds back. This further highlights the connection between that branch and the edge branch.

The numerical edge tracking was conducted using the two different grid resolutions R0 and R2. By focusing again on the observable  $a$ , better spatial convergence is observed for the edge branch than for the top branch in Fig. 19. This is a common observation in the shear flows: the edge state generally needs lower resolution than the corresponding turbulent solutions [38]. Despite slight differences both branches can be claimed to be qualitatively well captured numerically.

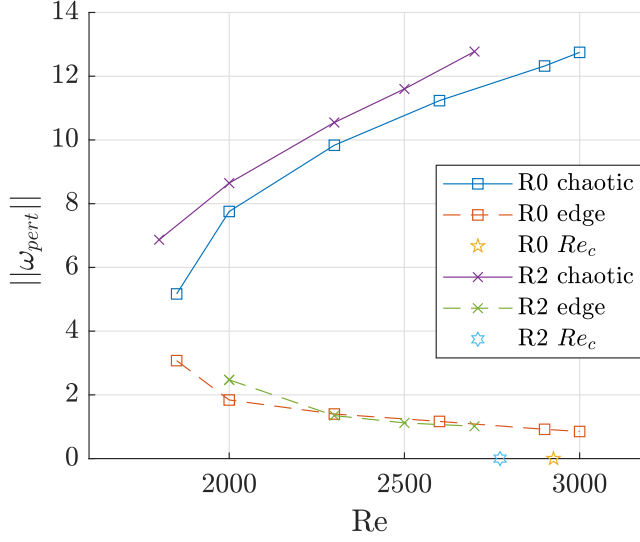


FIG. 19. Bifurcation diagram  $a(Re)$ . Edge state branch and chaotic branch obtained using time integration. Spatial resolutions R0 and R2. The critical value of  $Re_c$  corresponding to each resolution is shown using stars.

## VI. SUMMARY AND OUTLOOK

In this work the axisymmetric rotor-stator flow has been revisited, with the aim to explain the dynamical origin of the chaotic rolls reported in experiments and numerics for  $Re$  as low as 180 [6]. Former works by other authors suggested that the rolls could be a direct response of the rotor-stator system to imperfections inherent to the experiments, such as noise or permanent disturbances. Although we do not dismiss the possible role of external perturbations, we adopted here the point of view of bifurcation theory and looked instead for nonlinear branches of *self-sustained* solutions. The various branches of nonlinear solutions found contribute to a better global picture of the axisymmetric dynamics.

It was first shown using standard linear stability analysis that the axisymmetric base flow loses stability at a finite Reynolds number  $Re_c \approx 2900$ . At  $Re_c$  a Hopf branch of supercritical solutions emerges. This branch, difficult to continue numerically, was successfully captured using a harmonic balance method initialized by SCM, a method free from the use of timesteppers. The associated branch and its folds appear in all cases restricted to a very narrow  $O(1)$  interval of values of  $Re$ , and does not explain the subcriticality of the chaotic rolls.

Even though the bifurcation from the base flow appears supercritical, subcritical branches of axisymmetric finite-amplitude solutions have been identified. One of them is a branch of exactly periodic solutions, the other one is a branch of edge states separating the laminar and turbulent regimes. These two branches appear connected through a bifurcation scenario to be determined. They are unstable and exist down to  $Re = Re_{SN} \approx 1800$ . On one hand, this value of  $Re_{SN}$  is about 40% lower than the critical Reynolds number  $Re_c$ , which justifies the existence of subcritical rolls at least within this  $Re$  interval. On the other hand, this value of  $Re_{SN}$  is not low enough to explain the experimental observations.

The current results clarify the global *nonlinear* picture for the transition to chaos in axisymmetric rotor-stator flow. Branches of nonlinear invariant solutions exist in the range  $Re = 1800$ – $3000$  and were identified numerically using various techniques. Whether stable or unstable, they have little connection to experimentally observed rolls observed experimentally for  $Re = 200$ . The exact numerical values for the thresholds of each interval are indicative but were found to depend



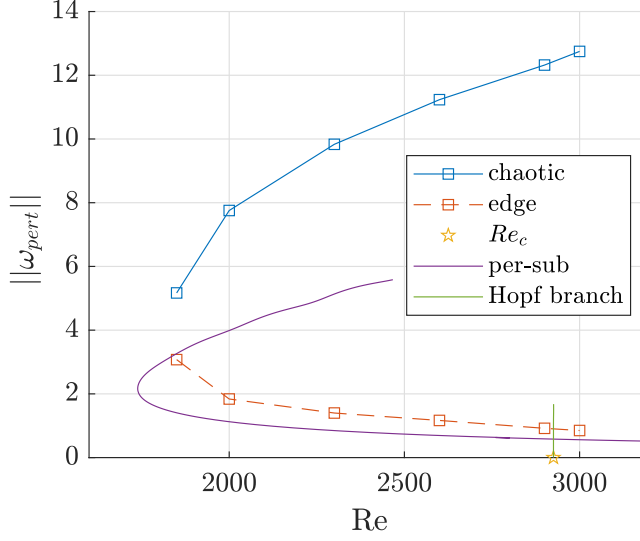


FIG. 20. Summary bifurcation diagram  $a(\text{Re})$ . Three different branches are shown: edge state branch together with the chaotic branch (red/blue squares), periodic-subcritical branch (purple solid line), and the Hopf branch arising at  $\text{Re}_c$  (green solid line). Spatial resolution R0.

moderately on the numerical resolution. The general picture is independent of the mesh resolution. The  $\text{Re}$  range can hence be conceptually divided into four separate regions as in Fig. 22:

(I) ( $0 \leq \text{Re} \lesssim 200$ ) The base flow is stable and no asymmetric sustained instability mode can occur neither in the experiments nor in the numerics.

(II) ( $\text{Re} = 200\text{--}1800$ ) The flow is stable both linearly and nonlinearly to axisymmetric perturbations. Sustained axisymmetric rolls can be observed in the experiments, but only as the result of continuous forcing by external perturbations. If such a forcing disappears, the flow relaminarizes. Some unstable or stable solutions with small attraction basin may exist but have not been found and, if any, are believed to play limited role in the dynamics.

(III) ( $1800 \lesssim \text{Re} \lesssim \text{Re}_c \approx 3000$ ) High-amplitude branches of self-sustained solutions exist and contribute to the formation of a chaotic set, possibly a chaotic attractor. Although the base flow is still linearly stable, strong enough perturbation can trigger chaotic rolls in the flow, linked to the existence of high-amplitude solutions. For infinitesimally small disturbance levels the system still responds to external excitations as if there were no finite-amplitude solutions.

(IV) ( $\text{Re} > \text{Re}_c \approx 3000$ ) The base flow is linearly unstable to axisymmetric perturbations. Infinitesimal perturbations to that base flow lead to unsteady rolls.

The branches of axisymmetric solutions found in the present work are summarized in the bifurcation diagram of Fig. 20. In Fig. 21 the individual solutions are depicted using a represen-

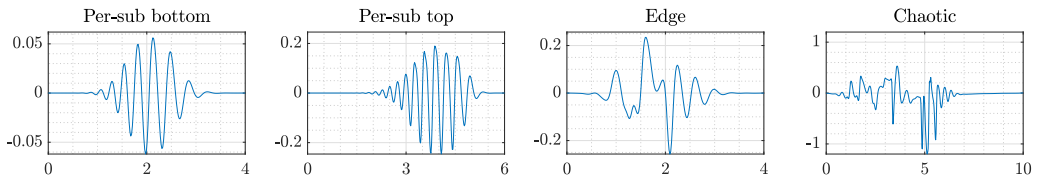


FIG. 21. Instantaneous radial profiles of  $u_\theta(r)$  at  $z = 0.9375$  for various solutions found at  $\text{Re} = 2300$ . From left to right: Periodic subcritical bottom branch, periodic subcritical top branch, Edge state and chaotic branch. Spatial resolution R0. The horizontal and vertical scales vary from subfigure to subfigure.

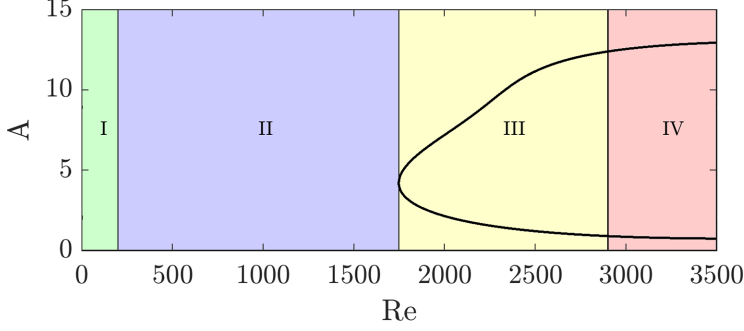


FIG. 22. Conclusion sketch from this study. Four different dynamical regions for axisymmetric rolls have been identified: (I) unconditionally stable base flow, (II) the base flow is stable but rolls appear as response to external forcing, (III) the base flow is only linearly stable but unstable to some finite-amplitude perturbations, chaotic rolls can be sustained without forcing, and (IV) chaotic rolls are sustained by the linear instability of the base flow. The solid black lines denotes finite-amplitude solutions described in this paper.

tative instantaneous radial profile of azimuthal perturbation  $u_\theta(r, z = 0.9375)$ . All profiles have in common the presence of a spatially growing wave in the decreasing radial direction, as it remains from the convective instability reported at smaller  $Re$ . The profiles from the periodic subcritical solution correspond to a simple localized wave packet localized in the self-similar region. They are all qualitatively similar to the critical eigenvector from Fig. 2, but the exact location of their geometric center within the Bödewadt layer varies. The radial profile of the edge state is spatially less organized than the previous wavepackets, it remains spatially localized but is now characterized by larger wavelengths. By comparison, the chaotic rolls (rightmost frame) have similar amplitude levels in the region closest to the axis but a more energetic core around  $r \approx 5$ , consistently with the description in Sec. V F.

The solutions from the Hopf branch, initially believed to be important for the subcritical dynamics, are restricted to a very narrow interval. They do not appear clearly connected to the other solutions and do not contribute to the origin of the chaotic rolls. The dynamical connections between the other different states found in this work are conjectured as relatively simple. The periodic subcritical states appear, upon increasing  $Re$ , in a saddle-node bifurcation. They do not bifurcate from the base flow, at least not in the range of  $Re$  investigated. The edge state branch results from one (or several) bifurcation(s) of the lower-branch of periodic subcritical states. The edge state is finally connected directly to the chaotic rolls via its linear instability. The fact that the whole subcritical dynamics appears fully disconnected dynamically from the base flow is common in open shear flows, it was also reported in rotor-stator flow by Lopez *et al.* for  $\Gamma = 5$  [9], for which no axisymmetric instability of the base flow was identified. The presence for  $\Gamma = 10$  of a critical point with a linear stability apparently leaves this picture unchanged. A radical difference between  $\Gamma = 5$  and 10 is the more complex dynamics observed for higher  $\Gamma$ . This is consistent with the qualitative sketch that wavelike perturbations, once born in the corner/shroud region, are advected radially inwards along the stator, and that the further they can travel from their origin, the more they get amplified and the more chaotic they become.

Natural extensions of the current work would concern in priority the intervals in  $Re$  labeled II and III. A possibility would be to conduct, in the spirit of [15], numerical simulations forced by noise, yet at lower values of  $Re$ . The exact role of the non-normality of the evolution operator linearized around the base flow deserves a deeper understanding, and could be quantified using resolvent analysis [51]. Besides, the dynamical role of the inertial waves present in the core of the cavity, their contribution to the transition process and to the individual nonlinear solutions deserve more investigation. Although the present study was focused on the influence of  $Re$  for a given geometry, the influence of the aspect ratio  $\Gamma = R/H$  of the rotor-stator cavity also needs to be addressed. In

particular, the influence of  $\Gamma$  on the linear stability threshold  $Re_c$  deserves more investigation. Eventually, experiments and numerics have shown that three-dimensionality can generally not be avoided due to the linear instability of the axisymmetric base flow to spiral modes. In the same spirit as the current study, the identification of unstable three-dimensional nonlinear solutions would be a relevant way, by reconstructing the state space of the system [52], to investigate the turbulent states observed in practice. These suggestions for future investigation are left for forthcoming studies.

### ACKNOWLEDGMENTS

The authors would like to thank L. S. Tuckerman for constructive discussions and E. Sleimi for the preliminary work on the subject as a part of his internship.

### APPENDIX: THRESHOLD SENSITIVITY TO THE NUMERICAL RESOLUTION

The sensitivity of the critical Reynolds number is addressed with respect to the numerical mesh and to the way the singular boundary conditions are treated numerically. Since the rotating shroud wall meets the stationary stator disk a discontinuity of the boundary condition for the azimuthal velocity is present in the associated corner. Such discontinuities are known to deteriorate the accuracy of spectral simulations, which has promoted the use of regularization techniques used in [9,10].

The sensitivity of the instability threshold is tested by using a series of meshes summarized in Table V and illustrated in Fig. 23, which reports the value of  $Re_c$  for each spatial discretization. Additionally, the influence of *regularizing* the corner singularity is also considered. This is achieved here by smoothing out the boundary condition at the Bödewadt corner, imposing an exponential velocity profile of the form  $u_\theta = r \exp(\frac{r-\Gamma}{\varepsilon})$ . Two regularizations have been considered:  $\varepsilon = 0.003$  and  $\varepsilon = 0.006$ . The case without any regularization ( $u_\theta = 0$ ) is referred to as  $\varepsilon = 0$  for ease of notation.

The spatial discretization of the governing equations and boundary conditions is second order accurate. It can be therefore expected that the value of  $Re_c$  also converges with the same order as the mesh is refined. The order of convergence for  $Re_c$  is estimated based on three different resolutions R2, R3, and R4 as

$$\text{order} = \log_{1.5} \left( \frac{Re_{c,R3} - Re_{c,R2}}{Re_{c,R4} - Re_{c,R3}} \right) \quad (A1)$$

The choice of the base 1.5 for the logarithm reflects the ratio between consecutive grids in Table V. As also noted in the Table, the order of convergence is close to 2.0, irrespective of the regularization used. Smoothing out the discontinuous boundary condition, although it affects quantitatively  $Re_c$ , does not affect the order of convergence. The dependence of  $Re_c$  on the regularization is due to

TABLE V. Critical Reynolds number  $Re_c$  depending on the spatial discretization. From R1 to R5 the ratio between two consecutive grid resolutions is 1.5 in each direction.

Resolution	$N_r$	$N_z$	Type	DOF	$\varepsilon = 0$	$\varepsilon = 0.003$	$\varepsilon = 0.006$
<b>R0</b>	<b>600</b>	<b>160</b>	Uniform	<b>390 k</b>	<b>2925.47</b>		
R1	683	128	Nonuniform	356 k	2963.41	2985.43	3035.61
<b>R2</b>	<b>1024</b>	<b>192</b>	Nonuniform	<b>796 k</b>	<b>2773.3</b>	2789.01	2826.55
R3	1536	288	Nonuniform	1.7 m	2697.48	2711.71	2746.33
R4	2304	432	Nonuniform	4.0 m	2663.96	2677.9	2711.97
R5	3456	648	Nonuniform	9.0 m	2648.9	2662.8	2696.8
			Extrapolation		2636.61	2650.59	2684.81
			Order		2.01	2.04	2.09

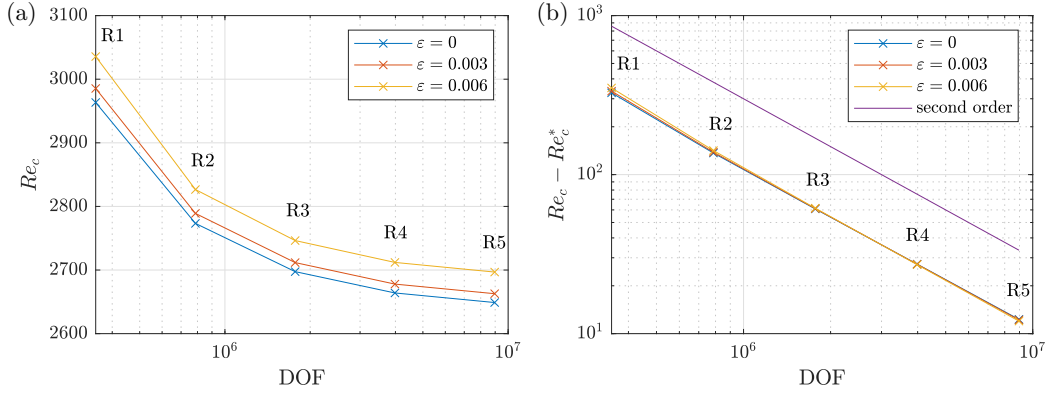


FIG. 23. (a) Critical Reynolds number  $Re_c$  depending on the spatial discretization in the case of regularized and nonregularized corner singularity. (b) Absolute error calculated using the Richardson extrapolated value  $Re_c^*$  compared with a second-order convergence curve.

the modification of the base flow linked to the modified boundary condition on the stator and not to the removal of the singularity. We conclude that using a discontinuous boundary condition does not deteriorate the results of the finite difference approximations used throughout this study. Similar conclusions were drawn for the lid-driven cavity, which also displays corner singularities; see, e.g., the recent review [53]. As a compromise the spatial resolution R2 with no corner regularization will provide meaningful results while requiring a manageable computational effort. As a computationally cheaper compromise spatial resolution R0 will also be extensively used. Both corresponding meshes are highlighted in bold in Table V.

- 
- [1] F. Moisy, T. Pasutto, G. Gauthier, P. Gondret, and M. Rabaud, Spiral patterns in swirling flows, *Europhys. News* **34**, 104 (2003).
  - [2] B. Launder, S. Poncet, and E. Serre, Laminar, transitional, and turbulent flows in rotor-stator cavities, *Annu. Rev. Fluid Mech.* **42**, 229 (2010).
  - [3] O. Dauchot and P. Manneville, Local *versus* global concepts in hydrodynamic stability theory, *J. Phys. II* **7**, 371 (1997).
  - [4] J. M. Lopez, Flow between a stationary and rotating disk shrouded by a co-rotating cylinder, *Phys. Fluids* **8**, 2605 (1996).
  - [5] L. Schouveiler, P. Le Gal, and M. P. Chauve, Instabilities of the flow between a rotating and a stationary disk, *J. Fluid Mech.* **443**, 329 (2001).
  - [6] G. Gauthier, P. Gondret, and M. Rabaud, Axisymmetric propagating vortices in the flow between a stationary and a rotating disk enclosed by a cylinder, *J. Fluid Mech.* **386**, 105 (1999).
  - [7] S. Poncet, E. Serre, and P. Le Gal, Revisiting the two first instabilities of the flow in an annular rotor-stator cavity, *Phys. Fluids* **21**, 064106 (2009).
  - [8] O. Daube and P. Le Qu  r  , Numerical investigation of the first bifurcation for the flow in a rotor-stator cavity of radial aspect ratio 10, *Comput. Fluids* **31**, 481 (2002).
  - [9] J. M. Lopez, F. Marques, A. M. Rubio, and M. Avila, Crossflow instability of finite B  dewadt flows: Transients and spiral waves, *Phys. Fluids* **21**, 114107 (2009).
  - [10] E. Serre, E. Tuluska-Sznitko, and P. Bontoux, Coupled numerical and theoretical study of the flow transition between a rotating and a stationary disk, *Phys. Fluids* **16**, 688 (2004).

- [11] A. Y. Gelfgat, Primary oscillatory instability in a rotating disk-cylinder system with aspect (height/radius) ratio varying from 0.1 to 1, [Fluid Dyn. Res.](#) **47**, 035502 (2015).
- [12] L. Schouveiler, P. Le Gal, and M. P. Chauve, Stability of a traveling roll system in a rotating disk flow, [Phys. Fluids](#) **10**, 2695 (1998).
- [13] N. Peres, S. Poncet, and E. Serre, A 3D pseudospectral method for cylindrical coordinates. Application to the simulations of rotating cavity flows, [J. Comput. Phys.](#) **231**, 6290 (2012).
- [14] E. Serre, E. Crespo Del Arco, and P. Bontoux, Annular and spiral patterns in flows between rotating and stationary discs, [J. Fluid Mech.](#) **434**, 65 (2001).
- [15] Y. Do, J. M. Lopez, and F. Marques, Optimal harmonic response in a confined Bödewadt boundary layer flow, [Phys. Rev. E](#) **82**, 036301 (2010).
- [16] P. Manneville, Transition to turbulence in wall-bounded flows: Where do we stand? [Mech. Eng. Rev.](#) **3**, 15-00684 (2016).
- [17] B. Eckhardt, Transition to turbulence in shear flows, [Physica A](#) **504**, 121 (2018).
- [18] S. Tobias, M. Proctor, and E. Knobloch, Convective and absolute instabilities of fluid flows in finite geometry, [Physica D](#) **113**, 43 (1998).
- [19] L. Martin Witkowski, I. Delbende, P. Le Quéré, and J. S. Walker, Axisymmetric stability of the flow between two exactly counter-rotating disks with large aspect ratio, [J. Fluid Mech.](#) **546**, 193 (2006).
- [20] A. Faugaret, Y. Duguet, Y. Fraigneau, and L. Martin Witkowski, A simple model for arbitrary pollution effects on rotating free-surface flows, [J. Fluid Mech.](#) **935**, A2 (2022).
- [21] J. L. Guermond, P. D. Mineev, and J. Shen, An overview of projection methods for incompressible flows, [Comput. Methods Appl. Mech. Eng.](#) **195**, 6011 (2006).
- [22] R. B. Lehoucq, D. C. Sorensen, and C. Yang, *ARPACK Users' Guide—Solution of Large-Scale Eigenvalue Problems with Implicitly Restarted Arnoldi Methods* (SIAM, Philadelphia, PA, 1998).
- [23] P. R. Amestoy, I. S. Duff, J. Y. L'Excellent, and J. Koster, A fully asynchronous multifrontal solver using distributed dynamic scheduling, [SIAM J. Matrix Anal. Appl.](#) **23**, 15 (2001).
- [24] V. Mantič-Lugo, C. Arratia, and F. Gallaire, Self-consistent mean flow description of the nonlinear saturation of the vortex shedding in the cylinder wake, [Phys. Rev. Lett.](#) **113**, 084501 (2014).
- [25] Y. Bengana and L. S. Tuckerman, Frequency prediction from exact or self-consistent mean flows, [Phys. Rev. Fluids](#) **6**, 063901 (2021).
- [26] J. Sierra-Ausin, V. Citro, F. Giannetti, and D. Fabre, Efficient computation of time-periodic compressible flows with spectral techniques, [Comput. Methods Appl. Mech. Eng.](#) **393**, 114736 (2022).
- [27] N. Cousin-Ritemard, O. Daube, and P. Le Quéré, Structuration de la solution stationnaire des écoulements interdisques en configuration rotor–stator, *C. R. Acad. Sci., Ser. II* **327**, 221 (1999).
- [28] D. Fabre, D. Sipp, and L. Jacquin, Kelvin waves and the singular modes of the Lamb–Oseen vortex, [J. Fluid Mech.](#) **551**, 235 (2006).
- [29] M. Avila, F. Mellibovsky, N. Roland, and B. Hof, Streamwise-localized solutions at the onset of turbulence in pipe flow, [Phys. Rev. Lett.](#) **110**, 224502 (2013).
- [30] V. Mantič-Lugo, C. Arratia, and F. Gallaire, A self-consistent model for the saturation dynamics of the vortex shedding around the mean flow in the unstable cylinder wake, [Phys. Fluids](#) **27**, 074103 (2015).
- [31] R. Seydel, *Practical Bifurcation and Stability Analysis*, Interdiscip. Appl. Math. Vol. 5 (Springer Science & Business Media, Cham, 2009).
- [32] E. L. Allgower and K. Georg, *Numerical Continuation Methods: An Introduction*, Springer Ser. Comput. Math. (Springer Science & Business Media, Cham, 2012), Vol. 13.
- [33] J. M. Chomaz, Global instabilities in spatially developing flows: Non-normality and nonlinearity, [Annu. Rev. Fluid Mech.](#) **37**, 357 (2005).
- [34] T. Khapko, T. Kreilos, P. Schlatter, Y. Duguet, B. Eckhardt, and D. S. Henningson, Edge states as mediators of bypass transition in boundary-layer flows, [J. Fluid Mech.](#) **801**, R2 (2016).
- [35] J. D. Skufca, J. A. Yorke, and B. Eckhardt, Edge of chaos in a parallel shear flow, [Phys. Rev. Lett.](#) **96**, 174101 (2006).
- [36] T. Itano and S. Toh, The dynamics of bursting process in wall turbulence, [J. Phys. Soc. Jpn.](#) **70**, 703 (2001).

- [37] Y. Duguet, P. Schlatter, and D. S. Henningson, Localized edge states in plane Couette flow, *Phys. Fluids* **21**, 111701 (2009).
- [38] J. Wang, J. Gibson, and F. Waleffe, Lower branch coherent states in shear flows: Transition and control, *Phys. Rev. Lett.* **98**, 204501 (2007).
- [39] Y. Duguet, A. P. Willis, and R. R. Kerswell, Transition in pipe flow: The saddle structure on the boundary of turbulence, *J. Fluid Mech.* **613**, 255 (2008).
- [40] T. Khapko, Y. Duguet, T. Kreilos, P. Schlatter, B. Eckhardt, and D. S. Henningson, Complexity of localised coherent structures in a boundary-layer flow, *Eur. Phys. J. E* **37**, 32 (2014).
- [41] T. M. Schneider, B. Eckhardt, and J. A. Yorke, Turbulence transition and the edge of chaos in pipe flow, *Phys. Rev. Lett.* **99**, 034502 (2007).
- [42] T. Khapko, T. Kreilos, P. Schlatter, Y. Duguet, B. Eckhardt, and D. S. Henningson, Localized edge states in the asymptotic suction boundary layer, *J. Fluid Mech.* **717**, R6 (2013).
- [43] J. M. Lopez, B. D. Welfert, K. Wu, and J. Yalim, Transition to complex dynamics in the cubic lid-driven cavity, *Phys. Rev. Fluids* **2**, 074401 (2017).
- [44] M. Beneitez, Y. Duguet, and D. S. Henningson, Modeling the collapse of the edge when two transition routes compete, *Phys. Rev. E* **102**, 053108 (2020).
- [45] Y. Bengana, J.-C. Loiseau, J.-C. Robinet, and L. Tuckerman, Bifurcation analysis and frequency prediction in shear-driven cavity flow, *J. Fluid Mech.* **875**, 725 (2019).
- [46] S. Thorpe, On standing internal gravity waves of finite amplitude, *J. Fluid Mech.* **32**, 489 (1968).
- [47] L. Oteski, Y. Duguet, L. Pastur, and P. Le Quéré, Quasiperiodic routes to chaos in confined two-dimensional differential convection, *Phys. Rev. E* **92**, 043020 (2015).
- [48] See Supplemental Material at <http://link.aps.org/supplemental/10.1103/PhysRevFluids.9.083903> for the movie of the transition from edge state to chaotic roll state and the movie of the temporal Fourier components of the edge state.
- [49] Y. Duguet, A. Willis, and R. Kerswell, Slug genesis in cylindrical pipe flow, *J. Fluid Mech.* **663**, 180 (2010).
- [50] T. M. Schneider and B. Eckhardt, Edge states intermediate between laminar and turbulent dynamics in pipe flow, *Philos. Trans. R. Soc. A* **367**, 577 (2009).
- [51] L. N. Trefethen, A. E. Trefethen, S. C. Reddy, and T. A. Driscoll, Hydrodynamic stability without eigenvalues, *Science* **261**, 578 (1993).
- [52] J. F. Gibson, J. Halcrow, and P. Cvitanović, Visualizing the geometry of state space in plane Couette flow, *J. Fluid Mech.* **611**, 107 (2008).
- [53] H. C. Kuhlmann and F. Romanò, The lid-driven cavity, in *Computational Modelling of Bifurcations and Instabilities in Fluid Dynamics*, edited by A. Gelfgat (Springer International Publishing, Cham, 2019), pp. 233–309.